Lung adventitial fibroblasts support type 2 Tregs to shape the response to influenza infection

Authors: Anthony A. Chang[1,2], Joanna Balcerek[2], Sofia E. Caryotakis[1,2], Kennedi B. Pyper[2], Peri Matatia[2,3], Elina B. Wells[2], Tatsuya Tsukui[8,9], Nathan A. Ewing-Crystal[1,2,4], Eric Dean Merrill[2], Nick M. Mroz[1,2,7], Madelene W. Dahlgren[2], Kelly M. Cautivo[2], Marcela T. Taruselli[2], Hiromi Nakao-Inoue[7], Anna V. Molofsky[5, 6, 7], Dean Sheppard[8,9], and Ari B. Molofsky[1,2,10]

Affiliations:

[1] Biomedical Sciences Graduate Program, University of California, San Francisco, San Francisco, CA, USA

[2] Department of Laboratory Medicine, University of California, San Francisco, San Francisco, CA, USA

[3] Immunology Graduate Program, Harvard University, Boston, MA, USA

[4] Medical Scientist Training Program, University of California, San Francisco, San Francisco, CA, USA.

[5] Neurosciences Graduate Program, University of California, San Francisco, San Francisco, CA, USA

[6] The Kavli Institute for Fundamental Neuroscience, and The Weill Institute for Neurosciences, University of California, San Francisco, San Francisco, CA, USA

[7] Department of Psychiatry, University of California, San Francisco, San Francisco, CA, USA

[8] Lung Biology Center, Department of Medicine, University of California, San Francisco, San Francisco, CA, USA

[9] Department of Medicine, Pulmonary Division, University of California, San Francisco, San Francisco, CA, USA

[10] Lead contact

Abstract:

Viral pneumonias are lung infections that lead to both short- and long-term complications, including acute respiratory distress syndrome (ARDS) and pulmonary fibrosis. Lung stromal–immune interactions balance pathogen clearance with excessive immune-mediated injury, and healthy lung repair with necessary scarring. Here, we define the lung spatiotemporal stromal-immune response to Influenza A virus (IAV) infection, focusing on the underappreciated role of fibroblasts and their dynamic states. We used 3D quantitative microscopy and scRNAseq to identify IAV-driven fibroblast states, including inflammatory fibroblasts, profibrotic fibroblasts, and adventitial fibroblasts (AFs). Unexpectedly, loss of fibroblast TGFβ signaling led to early enhancement of immuno-modulatory AFs, driving activation of tissue-resident type 2 regulatory T cells (T2-Tregs) and ultimately improving lung functional outcomes. In vitro co-culture systems additionally revealed that AFs act as a niche to support T2-Tregs. Our data suggest an intimate fibroblast-immune crosstalk is required to temporally and spatially balance lung tissue inflammation and repair.

Introduction:

Lung infections caused by common respiratory viruses are major drivers of human morbidity and mortality worldwide. Viral pneumonia poses a severe health risk, with 3-5 million severe cases reported annually worldwide from Influenza infections alone[1]. In both Influenza and COVID-19, acute respiratory distress syndrome (ARDS) is a prevalent complication. ARDS is driven by excessive inflammation caused by diverse lung insults, including pneumonia, trauma, environmental exposures, and systemic sepsis[2,3]. ARDS is characterized by acute lung endothelial and alveolar damage, pulmonary edema, hypoxemia, and multi-organ failure[4], and has a mortality rate of 25-50%[5,6]. In addition to acute sequelae, lung viral infections are linked to longer-term pulmonary complications, including pulmonary fibrosis, a process correlated with acute disease severity[7,8]. In COVID-19 patients, longitudinal studies identified long-term alterations in diffusion capacity in 40% of patients, with evidence of pulmonary fibrosis[9,10].

Organ fibrosis is driven by fibroblasts, a type of mesenchymal stromal cell that regulates and supports tissue structure and borders. However, fibroblasts are also increasingly implicated in immune responses, including those occurring within the lung[11,12]. Recent efforts have identified both cross-organ fibroblast states and organ-specific subsets. One conserved profibrotic, myofibroblast state, herein called fibrotic fibroblasts, expresses the highest levels of collagens, α-smooth muscle actin (αSMA), and Cthrc1^{+} (Collagen triple helix repeat containing 1), and, while rare in healthy adults, are a major driver of

pulmonary fibrosis[13–17]. In contrast to fibrotic fibroblasts, inflammatory fibroblasts often precede fibrotic fibroblast formation, are associated with acute tissue inflammation, and express Serum amyloid A 3 (Saa3)[18]. Both profibrotic and inflammatory fibroblast states are induced by lung perturbations and reflect discrete, conserved states. Under homeostatic conditions, two major fibroblast states exist in the lung: adventitial and alveolar fibroblasts. Adventitial fibroblasts (AFs) express markers such as Pi16 (Peptidase inhibitor 16), Col14a1 (Collagen type XIV alpha 1), and Ly6a (lymphocyte antigen 6 family member A) and play crucial roles in supporting lung airways, larger vessels, and immune cell subsets[21,22]. In contrast, alveolar fibroblasts specialize in supporting alveolar structure and gas exchange[23,24].

Just as fibroblast states are heterogeneous, so too are their respective immunological properties. While fibroblasts can express a multitude of cytokines and chemokines upon stimulation, not every fibroblast state possesses the same immune-modulatory profile[25–27]. AFs express the alarmins IL-33 and TSLP (thymic stromal lymphopoietin) and support lymphocytes associated with allergic type 2 inflammation, including ILC2s and Th2s[21]. In contrast, fibrotic fibroblasts are often immunosuppressive, directly suppressing $CD8^+$ T cell responses and limiting responses to checkpoint blockade in cancer[28,29]. Within secondary lymphoid organs such as lymph nodes and the spleen, lymphocyte-interactive fibroblasts called fibroblastic reticular cells (FRC) organize T-cell, B-cell, and dendritic cell interactions. Similar structures, named tertiary lymphoid tissue (TLT), also emerge in organs after inflammation. There is a clear spectrum of fibroblast states, each reflecting unique stromal cell positioning, function, and interplay with the immune system.

Regulatory T cells (Tregs) are crucial immunoregulatory lymphocytes in the immune response to influenza due to their suppressive and reparative function[30]. Tregs are major producers of IL-10 and TGFβ, which play prominent roles in local suppression of immune cells[31,32]. Similarly, production of amphiregulin (AREG) by Tregs is critical for the repair of type II alveolar lung epithelial cells (AT2s) during influenza infection. AREG drives repair in other tissues and is specifically produced by tissue-resident type 2-like (T2)-Tregs that express the IL-33 receptor IL1RL1 (ST2), the transcription factor GATA3, and other elements of the type 2 lymphocyte program[35–38]. An IL-33^+ fibroblast population supports T2-Tregs within visceral adipose tissue (VAT), skeletal muscle, and the oral mucosa. We previously identified an IL-33^+ AF state in the lung that serves as an immune hub for ILC2 and Th2 cells, suggesting that AFs may also support T2-Tregs[21,39–42]. Here, we show that lung AFs preferentially support T2-Tregs survival and function, serve as critical niche cells in vivo, and that modulation of this niche via TGFβ-signaling ultimately impacts Influenza A viral pneumonia.

115 **Results**:

116 **Lung immune topography in response to influenza infection**

117 First, we determined how lung immune cell positioning (i.e., topography) evolved during
118 Influenza A virus (IAV, strain PR8) infection (**Fig 1A**) using thick-section 3D confocal
119 microscopy. The lung is organized into two distinct regions: distal alveolar (parenchymal)
120 spaces and proximal bronchovasculature. Distal parenchyma is comprised of epithelial-
121 and microvascular-rich alveoli that specialize in gas exchange, whereas proximal
122 bronchovasculature includes large airways (bronchi, bronchioles, αSMA$^+$EpCAM$^+$), blood
123 vessels (αSMA$^+$EpCAM$^-$), neuronal innervation, lymphatic drainage (**Fig S1A-B**), and the
124 stromal cells (fibroblasts and mural smooth muscle cells) that support these
125 structures[43,44]. At rest (0 days post-infection/dpi), healthy alveolar type II epithelial cells
126 (AT2s, pro-SPC$^+$) were found throughout the distal lung parenchyma, with dispersed, low-
127 level immune cells (CD45$^+$) modestly enhanced in the adventitia **(Fig 1B)**. By 7 dpi,
128 immune cells expanded into alveolar areas, accompanied by a concomitant loss of AT2s,
129 consistent with lung damage and loss of functional regions of gas exchange **(Fig 1C)**. By
130 14 dpi, immune cells reached the distal areas of the lung and encompassed large
131 "damaged patches" **(Fig 1D)**. By 26 dpi, immune cells contracted into altered adventitial
132 spaces with increased TLT structures and with a concomitant increase in alveolar AT2s,
133 indicating lung functional recovery **(Fig 1E)**. Dysplastic epithelial patches, defined by
134 aberrant upper airway epithelial cell hyperplasia (Krt5$^+$), were sporadically noted at later
135 times post injury (**Fig S1C**)[45–47]. Lung IAV viral levels, as measured by nucleoprotein
136 transcript (*Np1*), were detectable as early as 3 dpi, peaked at 7 dpi, and were no longer
137 detectable by 9 dpi **(Fig 1F)**. In contrast, lung damage patches continued to enlarge from
138 7-14 dpi, but subsequently contracted by 26 dpi **(Fig 1G)**.
139
140 Next, we examined how lung lymphocyte subsets and their positioning changed during
141 IAV infection. After early innate- and myeloid cell-focused immune recruitment, influenza
142 drives a dominant anti-viral type 1 immune response, defined by an influx of lymphocytes
143 that produce IFNγ. In uninfected mice, we observed a homogeneous distribution of lung
144 type 1 lymphocytes (Tbet$^{ZsGreen+}$, T1Ls) **(Fig 1H)**, with a majority of T1Ls being
145 intravascular (**Fig S1D**). At 14 dpi, lung damage patches had accumulated T1Ls (**Fig 1I**),
146 many of which were tissue-resident cytotoxic T lymphocytes (ivCD45$^-$ CD8$^+$ Tbet$^+$) **(Fig**
147 **S1D-F,** 7-14 dpi**)**. Flow cytometry confirmed that tissue-resident IAV-driven lung T1Ls
148 were comprised of NK cells that peaked at 7 dpi and a mix of CD8 T cells and less
149 abundant Th1 CD4$^+$ T cells by 14 dpi (**Fig S1G**).
150
151 We then sought to determine the positioning of lung type 2 lymphocytes (T2Ls) after IAV
152 infection. T2Ls are traditionally associated with allergic inflammation, are enriched in
153 adventitial fibroblast-dense regions of the proximal lung[48,49], and have a context-

154 dependent impact on IAV infection outcomes[50–52]. Using a well-validated mouse reporter
155 line, we found effector T2Ls localized to expected lung bronchovascular adventitial
156 regions **(**IL5^{cre}; R26^{tdT} mouse, predominantly identifies ILC2s in resting mice; **Fig 1J)**[21].
157 By 14 dpi, there was a modest expansion and spread of ILC2s into damaged regions,
158 although they remained largely adventitial-localized **(Fig 1K)**. Treg subset(s) localize
159 closely with ILC2s in the lung[21,53], and indeed, Tregs were enriched within adventitial
160 spaces (Foxp3^{creERT2}; R26^{RFP} mice; **Fig 1L)**. After IAV infection, Tregs localized either to
161 the lung proximal bronchovasculature (adventitia) or along the borders of alveolar
162 damage patches surrounding dense patches of type 1 lymphocytes **(Fig 1M-N)**. Tregs
163 expanded over time, similar to other helper T cells, peaking at 14 dpi, whereas ILC2s
164 remained relatively stable **(Fig S1H)**. These data suggest that IAV drives distinct spatial
165 and temporal accumulation of type 1 versus type 2 and regulatory lymphocytes.
166

167 **Dynamic fibroblast topography in response to influenza infection**

168 Next, we examined lung stromal cell heterogeneity and evolution during IAV infection[54,55].
169 We found dynamic changes in lung αSMA levels and distribution up to 45 dpi, consistent
170 with altered stromal cells during IAV infection **(Fig S1I-K**). To better parse stromal cell
171 evolution during flu, we first focused on resting lung fibroblast states, confirming that Gli1^{+}
172 fibroblasts (enriched for AFs) were present at the tissue borders, including proximal
173 bronchovasculature and pleural surfaces **(**Gli1^{CreERT2}; R26^{tdT}; **Fig 2A, Fig 2SA)**. We
174 cross-validated these findings using reporter mice, which accurately identify the spatial
175 positioning of both AFs (Pdgfrα^{GFP+}Il33$^{mcherry+}$) and alveolar fibroblasts (Pdgfrα^{+}Il33^{-}) **(Fig.**
176 **2B)**. To further define the topography of lung fibroblast states, we used Xenium single-
177 cell spatial transcriptomics (10X Genomics), validating the predicted localization of AFs
178 and alveolar fibroblasts (**Fig 2C**). Using published single-cell RNA sequencing
179 (scRNAseq) of lung stromal cells **(Fig S2B)**, AFs (Col14a1^{+}Pi16^{+}) were further parsed
180 into two major subsets, marked by high *Il33* versus high *Aqp1*/*Adh7* **(Fig S2C)**[18]. Using
181 spatial transcriptomics, we found that Aqp1^{+} fibroblasts were preferentially located
182 immediately below the conducting airway epithelial cells and intercalated between airway
183 smooth muscle cells (note that Aqp1 also labels endothelial cells); in contrast, IL-33^{+} AFs
184 (Gli1^{+}IL-33^{+}) were localized farther from smooth muscle and were abundant around large
185 vessels and, to a lesser extent, outermost regions of airways **(Fig S2D-F),** identifying
186 them as the main immune-modulatory adventitial fibroblasts. We validated these findings
187 via thick-section microscopy **(Fig 2D, Fig S2G-J)**. These data suggest Aqp1^{+} AFs are a
188 subset of cells previously identified as sub-epithelial airway fibroblasts[17,56], whereas IL-
189 33^{+} AFs are preferentially associated with proximal vasculature and immune cell
190 networks, as we previously described[43] (**Fig S2K**).
191

After IAV infection, total adventitial volume expanded by 14 days post-IAV infection (**Fig 2E-F**), resembling AF expansion after lung helminth infection[21]. However, the relative localizations of the IL33^{+} adventitial fibroblasts and Aqp1^{+} sub-epithelial fibroblasts did not change **(Fig S2L-M).** After tissue injury or infection, several conserved and transient fibroblast states emerge, including inflammatory and pro-fibrotic states. Inflammatory fibroblasts (Saa3^{CreERT}; R26^{tdT}) were largely absent in the lungs of healthy mice. By 7 dpi, they were abundant within alveolar-damaged patches and sparsely present in adventitial regions. By 14 dpi, inflammatory fibroblasts decreased but remained localized to damage patches and the borders of altered adventitia **(Fig 2G)**. To characterize fibrotic fibroblasts, we used the lineage-tracing *Cthrc1* mouse line (Cthrc1^{CreERT}; R26^{tdT}). Fibrotic fibroblasts were sparse in the resting lung and were minimally induced by 7 dpi. By 14 dpi, fibrotic fibroblasts increased and were found in alveolar damaged patches, often at the interface of alveolar or adventitial regions (**Fig 2H**). Together, these data demonstrate lung fibroblast temporal and spatial heterogeneity after IAV infection, with the emergence of earlier inflammatory and later fibrotic fibroblast states within damaged lung patches, a pattern resembling changes observed in models of lung fibrosis[18] (**Fig 2I**).

Loss of fibroblast TGFβ signaling improves lung health during influenza infection

Lung fibrosis is a complication of severe respiratory virus infection[8,57,58], suggesting fibrotic fibroblasts may functionally contribute to lung remodeling after IAV infection. TGFβ is a key driver of the fibrotic fibroblast state in the lung, brain, and other tissues[59,20]. While an excess of fibrotic fibroblasts can drive fibrosis, a complete loss of this state can also be detrimental to organ functional recovery[17,20]. To test the functional role of fibrotic fibroblasts in IAV infection, we inducibly deleted TGFβ signaling within all fibroblasts (**Fig 3A**), hereafter called TGFbr2 conditional knockout mice (TGFbr2 cKO, Col1a2^{creERT2}; Tgfbr2$^{F/F}$ mice) and infected mice with IAV. It was previously observed that inducible deletion of fibroblast TGFβ signaling in adult TGFbr2 cKO mice did not impact animal health at rest[20]. However, after IAV infection, TGFbr2 cKO mice showed unexpectedly improved lung and overall health as early as 7 dpi, reflected by increased blood oxygen levels and body weight (**Fig 3B,C**). Viral titers at 3 dpi were not altered in TGFbr2 cKO mice, suggesting altered lung health was not directly linked to alterations in viral clearance **(Fig S3A)**.

To define the cellular dynamics underpinning lung functional improvements in TGFbr2 cKO mice, we performed lung single-cell RNA sequencing (scRNAseq) across the IAV infection time course (0, 3, 7, and 14 dpi), sorting and enriching for fibroblasts and T cells (**Fig S3B)**. Unsupervised clustering identified 6 broad cell subsets: lymphocytes, myeloid cells, stromal cells, endothelial cells, epithelial cells, and doublets **(Fig S3C,D)**. Sub-clustering on stromal cells identified several subsets, including alveolar fibroblasts (AlvF),

231 inflammatory fibroblasts, inflammatory/fibrotic transition fibroblasts, fibrotic fibroblasts,
232 adventitial fibroblasts (AF), and mural cells (pericytes/smooth muscle cells) (**Fig 3D**),
233 resembling findings after lung bleomycin-induced fibrotic injury[17,18]. AFs expressed
234 expected markers including *Pi16, Il33, Dcn, and Cd34*; inflammatory fibroblasts
235 expressed *Saa3, Ccl2, Ifit3, and Cxcl14;* fibrotic fibroblasts expressed profibrotic markers,
236 including *Cthrc1, Acta2, Fn1, and Tnc* (**Fig 3E**). Consistent with confocal microscopy,
237 inflammatory fibroblasts were present by 3 dpi, most prominent at 7 dpi, and decreased
238 by 14 dpi, whereas fibrotic fibroblasts were most prominent at 14 dpi; in contrast, both
239 subsets were largely absent at rest (**Fig 3F**).
240
241 Innate immune cells, such as neutrophils and NK cells, are critical early responders in
242 influenza infection[60–62]. Therefore, we investigated potential changes in both myeloid cells
243 and innate lymphoid cells after IAV in our TGFbr2 cKO animal scRNAseq. Within myeloid
244 populations, we identified dendritic cells (DCs), neutrophils, Arg1$^+$ macrophages,
245 monocytes, and other myeloid cells **(Fig S3E-G)**. Results showed small differences in the
246 relative proportions of myeloid cell subsets at both 3 dpi and 7 dpi **(Fig S3H-I)**. Flow
247 cytometry did not identify consistent alterations in PMN or NK cell number (see below,
248 **Fig S4A-D**). These data, along with comparable viral titers among TGFbr2 cKO and
249 control mice at 3 dpi, suggest that the observed lung health differences were not due to
250 altered viral clearance or neutrophil- or NK cell-mediated inflammation.
251
252 Next, we examined how TGFβ-signaling affected IAV-driven lung fibroblasts. As
253 expected, by 14 dpi TGFbr2 cKO mice had reduced fibrotic fibroblasts and a fibrosis
254 module score (**Fig 3G-J**). Although the diminution of fibrotic fibroblasts in TGFbr2 cKO
255 mice could, in theory, drive improved lung health, fibrotic fibroblasts did not develop until
256 later time points (~14 dpi), which did not correlate with improved animal health as early
257 as 7 dpi. This suggested that TGFbr2 cKO mice may have other changes in fibroblast
258 subsets, including potential shifts in AF states at earlier time points post-IAV infection.
259
260 To better parse AF subsets after IAV infection, we performed a second scRNAseq
261 experiment, enriching for stromal cells from the lungs of control and TGFbr2 cKO mice at
262 early time points post-IAV (0 dpi, 3 dpi, and 7 dpi). Unbiased clustering revealed 7 distinct
263 stromal cell states: Adventitial fibroblasts (AF), alveolar fibroblasts (AlvF), inflammatory
264 fibroblasts, pericytes, vascular- and peribronchial- smooth muscle cells (SMC), and
265 mesothelial cells **(Fig S3J-K)**. Unbiased sub-clustering was conducted on the AF cluster
266 **(Fig 3K)**, identifying expected Aqp1$^+$ sub-epithelial airway AFs and IL-33$^+$ AFs, as well as
267 Saa3$^+$ inflammatory AFs, and a Dpp4$^+$ AF state with similarities to fascial fibroblasts in
268 the skin (**Fig S3L-O**)[63] but distinct from mesothelial cells **(Fig S3P)**. By 3 dpi, AF subset
269 proportions were similarly abundant between cKO and control mice; however, cKO mice
270 displayed higher *Il33* gene expression across multiple AF subsets **(Fig 3L-M)**.

271 Furthermore, an IL-33$^+$ AF-derived module score (genes include *Il33, Ptgs2, Ccl11,* and
272 other AF-associated genes[17,21,64]) was applied to the various AF subsets, which showed
273 a higher score in the TGFbr2 cKO mice in the IL-33$^+$ AF state at rest **(Fig 3N)**; by 3 dpi,
274 this module was higher in TGFbr2 cKO mice across multiple AF states, although these
275 differences were no longer present by 7 dpi **(Fig 3O)**. These data suggest that loss of
276 fibroblast TGFβ signaling increased IL-33$^+$ AF immune-modulatory functionality at rest
277 and early time points after IAV, potentially underpinning the functional improvements in
278 IAV-infected cKO mice. More broadly, these findings suggest that TGFβ signaling in
279 fibroblasts exerts dual roles, driving the fibrotic fibroblast state but also directly restricting
280 the IL-33$^+$ AF immunomodulatory state and function.
281

282 **Type 2-like Tregs localize to the adventitial niche and expand in cKO mice after IAV**
283 **infection**

284 IL-33$^+$ AFs perform multiple functions, including maintenance and remodeling of the
285 adventitia, with similarities to IL-33$^+$ fascial fibroblasts at other natural tissue borders. IL-
286 33$^+$ AFs also regulate ILC2 and Th2 allergic lymphocytes that drive type 2
287 inflammation[21,65,66]. Lung ILC2s co-localize near Tregs and, during type 2 inflammation,
288 support Treg subset(s) that express portions of the "type 2 lymphocyte" program,
289 including the transcription factor Gata3 and the IL-33 receptor ST2 (IL1RL1)[53,67]. As such,
290 we hypothesized that the increase in IL-33$^+$ immunomodulatory AFs in TGFbr2 cKO mice
291 may alter lung Tregs or other adventitial immune cells, thereby contributing to improved
292 lung health after IAV infection. Indeed, using flow cytometry, we compared the immune
293 compartment of TGFbr2 cKO mice to littermate age-matched controls during IAV
294 infection, and found tissue-resident type 2 (T2) Tregs were elevated in cKO mice at 3 dpi
295 **(Fig 4A-B)**, with increased proliferation **(Fig 4C-D)**. We observed few differences in
296 frequencies of other immune cell subsets at rest, 3, 7, and 14 dpi, including: tissue
297 resident CD8$^+$ T cells, γδ T cells, ILC2s, macrophages, dendritic cells (DC1, DC2s),
298 alveolar macrophages, monocytes, neutrophils, eosinophils, and NK cells **(Fig S4A)**,
299 consistent with our scRNAseq data. Moreover, few differences were observed in
300 frequencies of specific subsets of tissue Type 1 Tregs and Type 1/2 CD4 effector cells
301 (**Fig S4B**). Little to no differences were observed between genotypes in the numbers of
302 the above-mentioned immune cells (**Fig SC-D**).
303

304 Next, we used our scRNAseq data to cross-validate the potential elevation of lung T2-
305 Tregs in cKO IAV-infected mice. Within the CD4$^+$ T cell cluster, we identified a small Treg
306 cluster and isolated it for further analysis **(Fig S4E**, clusters 0, 1, and 5**)**. A T2-Treg
307 module score (genes including *Gata3, Il1rl1, Areg, Setd2, Il2ra*) was elevated at both 3
308 dpi and 7dpi in TGFbr2 cKO Tregs as compared control Tregs **(Fig 4E)**. A Treg "type 1
309 immune module" score (including *Tbx21, Cxcr3, Cx3cr1*) showed no differences across

310 all time points post IAV infection, consistent with our flow cytometry data **(Fig 4F)**. We
311 conclude that T2-Tregs are preferentially activated early post-IAV infection in TGFbr2
312 cKO mice, coinciding with increased functionality of the immunomodulatory IL-33^{+} AF
313 state.
314
315 To further validate a Treg-AF relationship, we examined the localization of lung Tregs
316 using thick-section confocal microscopy in Treg-lineage-tracing mice (*Foxp3^{CreERT2};*
317 *R26^{RFP}*). We utilized intravenous labeling (IV) with either CD45 or Thy1.2 antibodies to
318 determine tissue residency. Tissue-resident Tregs (IV^{-}) localized preferentially to the lung
319 adventitia, whereas intravascular Tregs were broadly distributed in the alveolar
320 microvasculature **(Fig 4G-H, Fig S4F)**, resembling NK cells (Tbet^{+} CD3ε^{-}) that are
321 typically intravascular in unperturbed mice[68]. Using flow cytometry, we validated the
322 presence of a minor subset of tissue-resident Tregs in naïve mouse lungs **(Fig 4I)**. Next,
323 we parsed Treg states to identify type 2 (T2) or type 1 (T1) Tregs. We used a novel mouse
324 reagent that marks cells expressing the IL-33 receptor ST2 (IL1RL1) with GFP and
325 validated the expected GFP expression in ST2^{+} type 2 lymphocytes **(Fig 4J, Fig S4G)**.
326 T2-Tregs (*Foxp3^{creERT2}; R26^{RFP+}; ST2^{GFP+}*) were enriched within the tissue-resident lung
327 fraction and preferentially localized to the lung adventitia (**Fig 4K-M)** and in proximity to
328 putative ILC2s (ST2GFP^{+}; FoxP3^{-}) **(Fig S4H)**.
329
330 The temporal landscape of lung Treg subsets is dynamic after flu infection, and we
331 confirmed with flow cytometry that T2-Tregs were the most abundant early post-infection,
332 whereas T1-Tregs peaked by 14 dpi **(Fig S4I-J),** similar to published results[33,48]. To test
333 Treg localization relative to fibroblasts, we used PDGFRα^{GFP}; *Foxp3^{creERT2}; R26^{RFP}* mice.
334 As expected, tissue-resident Tregs localized tightly with PDGFRα$^{GFP\text{-}lo}$ AFs in adventitial
335 regions **(Fig 4N-O, Fig S4K)**. Additionally, Tregs were more closely associated with
336 immunomodulatory AFs (IL-33^{+}) compared to airway sub-epithelial AFs (Aqp1^{+}) **(Fig 4P-**
337 **Q)**. Together, these data suggest an early activation of adventitial-localized T2-Tregs in
338 cKO mice, which may explain the enhanced lung health outcomes, particularly given the
339 described beneficial roles of T2-Tregs in promoting epithelial repair through secretion of
340 Areg, production of IL-10, and local suppression of hyperactive immune cells[30,34,69,70].

341 **Lung adventitial fibroblasts directly and preferentially support T2-Tregs**

342 Given their spatial and temporal association, we predicted that lung IL-33^{+} AFs may
343 cross-regulate T2-Tregs. To better understand this putative stromal-immune interaction,
344 we developed a co-culture system using primary lung AFs and Tregs. AFs were sort-
345 purified (CD45^{-}CD31^{-}Pdgfra^{+}Sca1^{+}) and grown to confluence over 7 days, after which
346 Tregs were sort-purified from the spleen and lymph nodes of Foxp3^{GFP} reporter mice, and
347 added to AFs with or without exogenous TCR stimulation (**Fig 5A**). Tregs cultured with
348 AFs had higher viability, proliferation, and markers of a T2-state (ST2^{+}KLRG1^{+}),

349 resembling Tregs treated with TCR stimulation, and increased compared with media
350 alone controls (**Fig 5D-G**). In contrast to AFs, lung alveolar fibroblasts ($CD45^-CD31^-$
351 $Pdgfra^+Sca1^-$) induced less Treg proliferation **(Fig S5A)**. When Tregs were grown in
352 conditioned media from AFs, their proliferation remained low, similar to Treg-alone
353 conditions, albeit with a modest increase in T2-Treg markers ($ST2^+KLRG1^+$) (**Fig 5E-F**).
354 AF-conditioned media was sufficient to support Treg viability (**Fig 5G**), similar to previous
355 results demonstrating that AF-derived soluble factors can support ILC2s. Next, we co-
356 cultured Tregs with AFs in transwell plates and found reduced Treg proliferation and
357 viability (**Fig S5B-D**). Together, these data indicate that AFs can promote Treg viability,
358 proliferation, and "type 2" characteristics, acting primarily through contact-dependent or
359 local mechanisms, although AF-derived soluble signals may provide additional supportive
360 signals.
361
362 A traditional source of support is through Treg T cell receptor (TCR) signaling via MHC
363 class II from antigen-presenting cells, which could include AFs. However, purified AFs
364 from $MHCII^{-/-}$ mice were similarly able to support T2-Tregs in co-culture **(Fig S5E**). AFs
365 are also physiologic producers of IL-33, which we and others have shown supports type
366 2 lymphocytes[21,66]. To test how IL-33 may impact Treg support, we first added exogenous
367 IL-33 to the co-culture system. Although IL-33 by itself could not support Tregs, IL-33
368 synergized with AFs to better support T2-Tregs **(Fig S5F-I)**. To further test the role of IL-
369 33, wild-type and $IL\text{-}33^{-/-}$ AFs were sorted and found to support Tregs similarly (**Fig S5J-**
370 **K**), consistent with our previous work showing that AFs do not release IL-33 in vitro.
371 Together, these data indicate that while IL-33 is not required, it can work in concert with
372 other signals from AFs to amplify T2-Tregs.
373
374 Next, we sorted-purified effector Tregs ($CD44^+CD62L^-$) and naive Tregs ($CD44^-CD62L^+$)
375 and cultured them with AFs, finding that effector Tregs showed higher proliferation and
376 T2-like ($ST2^+KLRG1^+$) marker expression than their naive counterparts **(Fig S5L-M)**. To
377 further test AF support for Treg subsets, we sorted $ST2^+$ T2-Tregs and $ST2^-$ Tregs from
378 IL-33-injected mice for co-culture **(Fig 5H)**. We found that ex vivo T2-Tregs ($ST2^+$) had
379 higher proliferation and viability than their $ST2^-$ counterparts (**Fig 5I-J, Fig S5N**).
380 However, AFs did not induce T2-Treg gene expression ($ST2^+KLRG^+$) from purified $ST2^-$
381 Tregs. To further delineate if there was preferential AF support for T2-Tregs as compared
382 to T1-Tregs, we purified $Tbet^+$ and $Tbet^-$ Tregs from the lungs of IAV-infected mice at 14
383 dpi and used them in co-culture with AFs **(Fig 5K)**. T1-Tregs ($Tbet^+$) had reduced
384 proliferation and viability when cultured with AFs, compared to $Tbet^-$ Tregs (**Fig 5L-M**).
385 We conclude that AFs preferentially support pre-existing, or poised, effector T2-Tregs.
386
387 Universal fibroblasts were originally identified as a cross-tissue subset with increased
388 mesenchymal cell plasticity[22]. AFs and similar border/fascial fibroblasts are enriched for

389 this universal fibroblast state, and can adopt fibrotic fibroblasts, inflammatory fibroblast,
390 and lymphocyte-interactive (FRC-like) fibroblast states. We first investigated whether AFs
391 could adopt an inflammatory fibroblast state in vitro. We conducted RNA sequencing on
392 sorted AFs cultured with IL-1β, a signal known to drive this state[18]. We found that AFs
393 cultured with IL-1β had increased mRNA levels for genes associated with inflammatory
394 fibroblasts, including *Saa3* and *Ccl2* **(Fig S5O-P).** Next, we investigated whether AFs
395 could adopt a fibrotic fibroblast state. We cultured AFs at varying TGFβ concentrations
396 and performed bulk RNA sequencing. AFs showed a dose-dependent response to TGFβ,
397 with higher doses leading to increased expression of fibrosis-related genes, including
398 *Cthrc1, Fn1, Col1a1,* and *Col1a2;* however, all TGFβ doses resulted in a loss of AF-
399 associated immunomodulatory signature genes, including *Il33, Ptgs2, Tslp,* and *Ccl11*
400 **(Fig 5N, Fig S5Q-R)***.* To test whether TGFβ signaling directly impacted the support of
401 AFs for Tregs in vitro, we pre-treated AFs with TGFβ before seeding with effector Tregs
402 ($CD44^+$); AFs' ability to support Treg proliferation and viability was reduced (**Fig 5O-P**),
403 with a trend in reduction in T2-Treg markers ($ST2^+KLRG1^+$) **(Fig S5S)**. Overall, these
404 data suggest that AFs exposed to a range of TGFβ concentrations downregulate the AF
405 immunomodulatory program, whereas higher concentrations of TGFβ are required to
406 drive a profibrotic program **(Fig 5Q)**.
407

408 **Loss of T2-Tregs leads to exacerbated lung health in IAV infection**

409 To determine the functional role T2-Tregs may play during influenza infection, we used
410 T2-Treg-deleter mice ($Foxp3^{creERT2}$; $R26^{RFP}$; $Gata3^{F/F}$). Of note, non-inducible versions of
411 this mouse strain have been previously used in other mouse models[34,71], although Treg
412 Gata3 expression during thymic development may have influenced these phenotypes.
413 We first validated the mouse model by injecting tamoxifen intraperitoneally and analyzing
414 lungs 14 days later **(Fig. 6A)**. As expected, we saw a specific and sensitive loss of T2-
415 Tregs marked by Gata3, ST2, and KLRG1 **(Fig 6B-F)**, without overt signs of mouse
416 autoimmunity**.** In contrast, no differences in frequencies or total numbers of tissue
417 resident Tregs, $CD4^+$ effector, and $CD8^+$ effector T cells were observed (**Fig S6A-C**),
418 suggesting a specific impact on T2-Tregs. After IAV infection, T2-Treg deleter mice
419 showed consistent loss of T2-Tregs from 3 dpi to 14 dpi (**Fig 6G-H**). Loss of T2-Tregs led
420 to exacerbated lung health, as measured by both peripheral blood oxygen levels and
421 body weight **(Fig 6I-J)**. Other immune cell populations, including tissue-resident $CD8^+$ T
422 cells, tissue-resident type 1-like Tregs, αβ T cells, ILC2s, macrophages, alveolar
423 macrophages, monocytes, neutrophils, eosinophils, and NK cells, were not different
424 between the groups (**Fig. S6D-N**). These data show that T2-Tregs play a significant role
425 in protecting lung health during IAV infection and suggests that elevated T2-Tregs in
426 TGFβr2 cKO mice are responsible for improved lung function (**Fig. S6P**).

427 **Discussion**:

428 Here, we uncovered a functionally critical lung adventitial fibroblast – T2-Treg niche.
429 Increased functionality of immunomodulatory AFs, driven by reduced TGFβ signaling, led
430 to early activation and expansion of type 2-like (T2) tissue Tregs, ultimately improving
431 lung health in a mouse model of viral influenza. Fibroblasts are heterogeneous and
432 functionally malleable, with recent work delineating diverse, conserved fibroblast states
433 including (1) *Cthrc1*$^{+}$ profibrotic fibroblasts, (2) *Pi16*$^{+}$ adventitial/border fibroblasts, (3)
434 *Saa3*$^{+}$ inflammatory fibroblasts, and (4) *Ccl19*$^{+}$ lymphocyte-interactive fibroblasts that
435 resemble fibroblastic reticular cells (FRC) in the lymph nodes and spleen. Each fibroblast
436 state plays a unique role in local tissue homeostasis, injury, repair, and disease[17,18,43,72].
437 While tools such as scRNAseq have helped uncover fibroblast heterogeneity, the state-
438 specific spatial-temporal positioning, regulation, and functional contributions of fibroblasts
439 remain unclear. Using a combination of genetic tools, scRNAseq, and thick-section 3D
440 confocal imaging, we defined the fibroblast state positioning within the lung at rest and
441 after Influenza A virus infection. Saa3^{+} inflammatory fibroblasts developed early after IAV
442 infection and were predominantly confined to damaged lung regions. Profibrotic Cthrc1^{+}
443 fibroblasts developed later during influenza infection, were dependent on TGFβ signaling,
444 and were located at the interface between damaged and healthy lung tissue. We also
445 found unexpected heterogeneity in adventitial fibroblasts after viral infection. These
446 include validation of sub-epithelial airway-associated AFs (Aqp1/Adh7+), perivascular IL-
447 33^{+} immunomodulatory AFs, and the emergence of IAV-driven inflammatory (Saa3^{+}) AF
448 states that localize to the adventitial borders. In addition to the role of TGFβ in promoting
449 fibrotic fibroblasts, we uncovered a secondary role in limiting IL-33^{+} AFs. Preventing
450 TGFβ signaling in immunomodulatory AFs preserved their functional capacity during IAV
451 infection, leading to increased T2-Tregs and improved viral pneumonia outcomes.
452
453 Our findings highlight the role of immunomodulatory AFs in supporting tissue-resident T2-
454 Tregs. T2-Tregs are a Treg state that is enriched within resting tissues and can play
455 beneficial roles (e.g., wound repair) or pathologic roles (e.g., cancer). Thick-section
456 microscopy revealed that lung T2-Tregs localize preferentially to adventitial spaces near
457 immunomodulatory IL-33^{+} AFs. Co-culture experiments demonstrated direct, preferential
458 support by AFs for T2-Tregs, which synergizes with IL-33 signaling. Although AFs in vitro
459 did not release IL-33, they can be relevant in vivo sources of IL-33, and this pathway likely
460 represents one mechanism by which AFs regulate T2-Tregs. How AFs support T2-Treg
461 survival and proliferation remains to be elucidated, but involves contact-dependent
462 mechanisms, potentially including ECM-integrin and TNF superfamily receptor-ligand
463 interactions. Interestingly, Treg support remains unique to the traditional
464 immunomodulatory AFs, as profibrotic (TGFβ-treated) AFs lost their Treg-supportive
465 capacity. This is also reflected in vivo, where inducible loss of fibroblast TGFβ signaling

466 TGFbr2 cKO mice) led to enhanced immunomodulatory AFs and increased T2-Treg
467 activation, ultimately improving lung health.
468
469 While we have demonstrated TGFβ can impact AF support of T2-Tregs, the cellular
470 source and activators of TGFβ were not defined. Myeloid cells, such as macrophages, as
471 well as Tregs themselves, are traditional sources of TGFβ[73]; however, TGFβ is secreted
472 as a latent complex consisting of active TGFβ and the latency-associated peptide (LAP).
473 Binding of LAP to integrins, including lung αvβ6 and αvβ8[74–76], allows TGFβ to bind to its
474 cell surface receptors and induce signaling. Tregs play crucial functional roles by
475 activating TGFβ via αvβ8[77,78]. Therefore, while AFs directly support Tregs, we speculate
476 that TGFβ activation from Tregs themselves plays a significant role in the local cross-
477 regulation of AF function, thereby more broadly impacting adventitial immune "hubs". T2-
478 Tregs are well recognized for contributing to improved tissue health, with published
479 mechanisms including enhanced immunosuppression and tissue repair via amphiregulin
480 and IL-10 production. Our results show that the inducible loss of T2-Tregs led to reduced
481 lung health after influenza infection, further highlighting the broader importance of T2-
482 Tregs. Collectively, our data illustrate the diversity of lung fibroblast states after viral
483 pneumonia and the crucial role of AFs in modulating key immune cells, such as Tregs, to
484 preserve lung health. Modulation of fibroblast states, including the key role of AFs and
485 their immunomodulatory properties, represents a promising future therapeutic target.
486

487 **Figure Legends**:

488 *Figure 1:*
489 **A,** Schematic illustrating the influenza model of infection in the lung. **B-E**, Time course
490 whole slice and zoomed images of (**B**) 0 dpi, (**C**) 7 dpi, (**D**) 14 dpi, and (**E**) 26 dpi mouse
491 lung stained for AT2s (pro-SPC) and immune infiltrate (CD45). **F**, Time course of viral
492 load using qPCR quantitation of viral nucleoprotein (NP-1). **G**, Time course of relative
493 damage patches ($CD45^{+}proSPC^{-}$ regions) in lung slices. **H-I**, Whole slice and zoomed
494 image of T1L ($Tbet^{ZsGreen+}$) localization at (**H**) 0 and (**I**) 14 dpi. **J-K**, Whole slice and
495 zoomed images of ILC2 ($IL5^{cre}$; $Rosa26^{tdt+}$) localization at (**J**) 0 dpi and (**K**) 14 dpi. **L-M**,
496 Thick section and zoomed images of Treg ($Foxp3^{creERT2}$; $Rosa26^{RFP+}$) localization at (**L**)
497 0 dpi and (**M**) 14 dpi. **N**, Representative image of Treg ($Foxp3^{creERT2}$; $Rosa26^{RFP+}$) and
498 T1L ($Tbet^{ZsGreen+}$) localization within a damage patch. **B-E**, **H-M**, 20-40 μM slices. **N,** 200-
499 300μM slices; images represent two or more mice. **G**, Graph shows mean±s.d. *$p<0.05$,
500 ***$p<0.001$; one-way ANOVA, Tukey post-test.
501

502 *Figure S1:*
503 **A**, Thick section imaging illustrating localization of lymphatics ($Lyve1^{+}$) and sensory
504 neurons ($Nav1.8^{+}$). **B**, Thick section imaging and Imaris surfaces illustrating blood

(αSMA$^+$EpCAM$^-$) and airway (αSMA$^+$EpCAM$^+$) vasculature at 0 dpi. **C**, Thick section imaging and Imaris surfaces illustrating the development of dysplastic patches at both 14 and 27 dpi. **D**, Thick section imaging of expansion and contraction of CD8 T cells (CD8^{cre}; Rosa26^{tdt}; Tbet^{ZsGreen} reporter mice) across timepoints after influenza infection (left panels), and of expansion of IV$^-$ CD8 T cells between 0 and 14 dpi (right panels). **E**, Thick section imaging illustrating expansion and contraction of Tbet$^+$ (green) vs. Tbet$^-$ (magenta) CD8 T cells across timepoints after influenza infection. **F**, Quantitation from thick section imaging illustrating standardized numbers and frequencies of CD8 cells across influenza time course. **G-H**, Flow cytometry data measuring numbers of (**G**) NK, CD8, and CD4 (CD4$^+$Foxp3$^-$) and (**H**) Tregs, and ILC2s across timepoints after influenza infection. **I**, Thick section imaging identifying de novo αSMA generation (αSMA^{dim}) versus traditional vasculature (αSMA^{bright}) at 14 dpi. **J**, native staining of αSMA in thick section imaging across influenza infection. **K**, Quantification of de novo αSMA surfacing across influenza infection. **A-E**, and **I-J**, 200-300μM slices; images represent 2 or more mice.

Figure 2:

A, Representative whole slice and zoomed image detailing adventitial regions (Gli1$^+$) labeled by the *Gli1* lineage tracer (Gli1^{creERT2}; Rosa26^{tdt}). **B**, Representative whole slice and zoomed image detailing localization of AFs (Pdgfra^{GFP+}Il-33$^{mcherry+}$) and alveolar fibroblasts (AlvFs, Pdgfra^{GFP+}Il-33$^{mcherry-}$). **C**, Representative whole slice and zoomed image of Xenium spatial sequencing detailing relative localizations of AFs (magenta), AlvFs (cyan), goblet cells (grey), and smooth muscle (blue) cells. **D**, Representative image of Imaris surfaces detailing blood vessels (red) and airway (blue) vasculature in relation to sub-epithelial airway AF surfaces (white). **E**, Thick section and zoomed image of adventitial spaces (white dashed line) marked by Pi16 staining at 0 dpi and 14 dpi. **F**, Imaris quantitation of adventitial thickness from thin section stacks. **G**, Time course images looking at the presence and localization of inflammatory fibroblasts (Saa3^{creER}; Rosa26^{Ai14+}) at 0, 7, and 14 dpi. Thick-section native imaging of inflammatory fibroblasts (left panels), and adventitial regions (Pi16$^+$) and immune cells (CD45$^+$, right panels). **H**, Time course images looking at the presence and localization of fibrotic fibroblasts (Cthrc1^{creER}; Rosa26^{Ai14+}) at 0, 7, and 14 dpi. Thick-section native imaging of fibrotic fibroblasts (left panels), and alveolar regions (pSPC$^+$) and immune cells (CD45$^+$, right panels). **I**, Schematic illustrating changes in immune-fibroblast population dynamics and localizations over the course of influenza infection. (**A-C,** and **G)**, 20-40μM slices. (**D-E,** and **H)**, 200-300μM slices; images represent two or more mice. (**F**) Graph shows mean±s.d. ****$p<0.0001$; paired Student's T-test.

Figure S2:

A, Thick section and zoomed image of adventitial spaces marked by Gli1 lineage tracing (white dashed line). **B**, UMAP plot (Tatusya et al., 2024) demarcating various cell populations sorted from healthy and bleomycin-treated mice. **C**, UMAP plot and volcano plot illustrating transcriptional differences between IL-33$^+$ and Aqp1$^+$ AFs. **D**, UMAP plot of total Xenium spatial sequencing data illustrating the location of clusters of alveolar (Scube2$^+$) and adventitial (Pi16$^+$) fibroblasts. **E**, Magnified spatial sequencing image illustrating differences of *Aqp1* transcript (yellow) overlap over AFs (magenta) between airway (left panel) and blood vessel (right panel) regions. **F**, Magnified spatial sequencing image illustrating differences of *Il33* (green) transcript overlap over AFs (magenta) between airway (left panel) and blood vessel (right panel) regions. **G**, Imaris surfaces looking at relative localizations of Aqp1$^+$ (white) and Aqp1$^-$ (magenta) AFs to αSMA (left panel) with native staining of Gli1 lineage tracer (magenta, top right) and Aqp1 (white, bottom right). **H**, Imaris surfaces showing relative localizations of IL-33$^+$ (white) and IL-33$^-$ (magenta) AFs to αSMA (left panel), with native staining for the Gli1 lineage tracer (magenta, top right) and IL-33 (green, bottom right). **I**, Imaris quantitation illustrating frequency of Aqp1$^+$ and Aqp1$^-$ surfaces that are less than 20μM from identified airways (using DAPI method). **J**, Imaris quantitation illustrating average distances of Aqp1$^+$ and IL-33$^+$ AFs to αSMA. **K**, Graphical illustration showing differential localization of Aqp1$^+$ and IL-33$^+$ AFs within the adventitia. **L**, Time course series of images looking at 0, 7, and 14 dpi timepoints of airway-associated (Gli1$^+$Aqp1$^+$) AFs. Left panels illustrate Imaris surfaces showing αSMA surfaces (blue) and airway-associated AF surfaces (white). Right panels illustrate native immunofluorescence (IF) and reporter staining of overlapping Gli1 staining (magenta) and Aqp1 staining (sky blue) in adventitial regions (white dashed line). **M**, Time course series of images looking at 0, 7, and 14 dpi timepoints of immune-modulatory (Gli1$^+$IL-33$^+$) AFs. Left panels illustrate Imaris surfaces showing αSMA (blue) and immune-modulatory (white) surfaces. Right panels illustrate native immunofluorescence (IF) and reporter staining of overlapping Gli1 staining (magenta) and IL-33 staining (green) in adventitial regions (white dashed line). (**A, G-H, L-M**) 200-300μM slices. (**E-F**) 20-40μM slices; images represent two or more mice. (**I-J**) Graph shows mean±s.d. ****$p<0.0001$; paired Student's T-test.

Figure 3:

A, Graphical diagram illustrating mouse model and timing of tamoxifen injections (i.p.), influenza inoculation (i.n.), and sacrifice. **B**, Pulse oximetry time course in controls/TGFbr2 cKOs (left). Pulse oximetry measurements at 7 dpi comparing controls and TGFbr2 cKOS (right).**C**, Body weight time course in controls/ TGFbr2 cKO mice (left). Body weight measurements at 7 dpi comparing controls and TGFbr2 cKO mice (right). **D**, UMAP of fibroblast clusters showing various fibroblast states, including alveolar,

585 inflammatory, “inflammatory-fibrotic” transition, profibrotic, adventitial, and pericytes. **E**,
586 Dot plot showing marker genes for all cellular clusters. **F**, UMAP of fibroblast clusters
587 illustrating timepoint metadata. **G-H**, UMAP of respective genotype fibroblast clusters
588 comparing (**G**) controls to (**H**) TGFbr2 cKOs. **I**, Quantitation of normalized proportion of
589 the fibrotic fibroblast cluster between control (red) and TGFbr2 cKO (blue) mice. **J**,
590 Fibrosis module score (upregulated genes that are associated with a pro-fibrotic
591 phenotype) on total fibroblast cluster between control and TGFbr2 cKO mice at 14 dpi. **K**,
592 UMAP of reclustered adventitial fibroblasts illustrating various AF states, including
593 immune-modulatory IL-33$^+$, sub-epithelial airway Aqp1$^+$, fascial-like Dpp4$^+$, inflammatory-
594 transition, and inflammatory-like. **L-M**, UMAP plots showing *Il33* gene expression at 3 dpi
595 in (**L**) control and (**M**) TGFbr2 cKO AFs. **N**, IL-33 functionality scores (genes associated
596 with immune-modulatory capacity of IL-33$^+$ AFs) applied across the following AF states:
597 immune-modulatory, fascial-like Dpp4$^+$, airway-associated, and inflammatory-like at 3
598 dpi. **O**, Table illustrating IL-33 functionality comparisons across 0, 3, and 7 dpi. Graphs
599 show mean±s.d. ns = not significant, **p<0.01, ***p<0.001, ****p<0.0001; Mixed-effect
600 analysis with Geisser-Greenhouse correction (**B-C, left panels**); Student’s T-test (**B-C,**
601 **right panels**); Mann-Whitney test (**J, N-O**).
602
603 *Figure S3*:
604 **A**, qPCR quantitation of 3 dpi viral levels using NP-1 primers between control and cKO
605 mice. **B**, Graphical illustration of scRNAseq experiment. Sorting strategy: 5 populations
606 of cells were sorted in equal numbers and combined for sequencing: CD4 T cells
607 (CD3$^+$CD4$^+$), Total lymphocytes (CD45$^+$Thy1.1$^+$), Myeloid cells (CD45$^+$Thy1.1$^-$), Stromal
608 cells (CD45$^-$PDGFRα^+) and other lineage negative structural cells (CD45$^-$ PDGFRα^-). All
609 littermate mice were infected on the same day and harvested at 0, 3, 7, and 14 dpi. **C-D**,
610 Dot plot (**C**) and UMAP (**D**) illustrating the various cell populations sorted out:
611 Lymphocytes, myeloid, fibroblasts, endothelial, epithelial, doublets, and the marker genes
612 for all cellular clusters. **E-F**, Dot plot (**E**) and UMAP (**F**) identifying various myeloid cell
613 populations (**F**): Monocytes, interstitial macrophages, IFN-responsive monocytes, Arg1$^+$
614 macrophages, lipid-associated macrophages, neutrophils, alveolar macrophages,
615 inflammatory macrophages, dendritic cells, and circulatory monocytes, and their marker
616 genes. **G**, UMAP of myeloid clusters illustrating timepoint metadata. **H**, Pie chart showing
617 relative proportions of all identified myeloid cells comparing control to TGFbr2 cKO mice
618 at 3 and 7 dpi. **I**, Pie chart showing relative proportions of all identified innate lymphoid
619 cells (NK cells, $\gamma\delta$ T cells, and ILC2s) comparing control to TGFbr2 cKO mice at 3 and 7
620 dpi. **J-K**, Global UMAP (**J**) and (**K**) Dot plot illustrating the various cell populations sorted
621 out: mesothelial cells, alveolar fibroblasts, adventitial fibroblasts, inflammatory fibroblasts,
622 pericytes, smooth muscle cells, peribronchial (sub-epithelial) fibroblasts, epithelial cells,
623 and doublets, and their marker genes. **L-O**, UMAP representation of (**L**) IL-33 immune-
624 modulatory module score, (**M**) *Dpp4* gene expression, (**N**) Aqp1$^+$ airway-associated

module score, and (**O**) inflammatory module score. **P**, Volcano plot comparing DEGs between traditional mesothelial cluster and fascial-like Dpp4^{+} AF cluster. ns = not significant; Student's T-test (**A**).

Figure 4:

A, Quantitation comparing frequency (left panel) and numbers (right panel) of type 2-like (ST2^{+}) tissue resident Tregs between control (white) and TGFbr2 cKO (red) mice. **B**, Representative FACS plot showing differences in ST2 and KLRG1 expression in tissue resident Tregs between control and TGFbr2 cKO mice. **C**, Quantitation comparing frequency (left panel) and numbers (right panel) of proliferating (Ki67^{+}) type 2-like tissue resident Tregs between control (white) and TGFbr2 cKO (red) mice. **D**, Representative FACS plot showing differences in Ki67 expression in type 2-like tissue resident Tregs between control and TGFbr2 cKO mice. **E-F**, Module scores looking at type 2 (**E**) and type 1 (**F**) characteristics of the Treg population across 3, 7, and 14 dpi. **G**, Thick-section image illustrating Imaris surfaces of adventitial (white) and parenchymal (red) tissue-resident Tregs. **H**, Quantitation comparing proportions of tissue resident and parenchymal Tregs that are adventitial-associated (<20μM from αSMA). **I**, Representative FACS plot validating CD45i.v. staining. **J**, FACS plots illustrating the specificity of ST2 expression of the ST2^{GFP} reporter across various immune cells. **K**, Thick-section image illustrating Imaris surfaces of tissue resident type 2 Tregs (magenta) and intravascular type 2 Tregs (green). **L**, Quantitation comparing proportions of tissue resident and intravascular Type 2-like Tregs that are adventitial-associated (<20μM from αSMA). **M**, Representative FACS plot validating ST2^{GFP} expression within Tregs. **N**, Representative thick section and zoomed image of native imaging looking at relative localizations of AFs (PDGFRα^{low}) and Tregs (Foxp3^{creERT2}; Rosa26^{RFP+}). **O**, Imaris quantification of average distance of intravascular (IV^{-}) and tissue resident (IV^{+}) Tregs to PDGFRα^{low} AFs. **P**, Zoomed image of Imaris surfaces looking at relative localizations of Tregs (green) and IL-33^{+} cells (magenta). **Q**, Imaris quantitation of average distance of Aqp1^{+} AFs, IL-33^{+} AFs, and tissue resident Tregs to αSMA. (**G, K, N, P**) 200-300μM slices; images represent two or more mice. Graphs show mean±s.d. ns = not significant, *p<0.05, **p<0.01, ***p<0.001, ****p<0.0001; Student's T-test (**A, C, H, L, O**); Mann-Whitney test (**E-F**). One-way ANOVA, Tukey post-test (**Q**).

Figure S4:

A-D, Tables illustrating values of time course flow cytometry data looking at frequencies (**A-B**) and cell number (**C-D**) of various immune cells between control and TGFbr2 cKO mice at rest, 3, 7, and 14 dpi. **E**, UMAP illustrating filtered and re-clustered CD4^{+} cells and *Foxp3* expression for Tregs. **F**, Representative imaging of CD45/Thy1.2i.v. labeling illustrating intravascular Tregs (i.v.$^{+}$, top right) and tissue resident Tregs (i.v.$^{-}$, bottom

665 right). **G**, Graphical illustration of ST2^{GFP} reporter construct. **H**, Thick-section native
666 imaging illustrating type 2 Tregs (ST2^{GFP+}Foxp3^{creERT2}; Rosa26^{RFP+}, white arrows). **I**,
667 Serial UMAPS illustrating *Tbx21* and *Il1rl1* expression in Tregs over time after influenza.
668 **J**, FACS data illustrating frequencies of Type 1 (blue) and Type 2 (purple) Tregs at rest,
669 3, 7 and 14 days post influenza infection. **K**, Representative image showing Imaris
670 surfacing of PDGFRα^{lo} cells (green) and Tregs (magenta). Graphs show mean±s.d.;
671 Student's T-test for each time point (**A-D**). (**F, H, I**) 200-300μM slices; images represent
672 two or more mice.
673
674
675 *Figure 5*:
676 **A**, Graphical illustration of *in vitro* co-culture procedure. **B**, Representative FACS plot
677 showing the effect of AFs on ST2 and KLRG1 expression on Tregs. **C**, Representative
678 plot showing effect of AFs on Treg proliferation (CTV staining). **D**, Graphical illustration
679 illustrating total spleen and nodal Tregs sorted for culture from Foxp3^{eGFP} mice. **E-G**,
680 Quantitation comparing the effects of a combination of AFs, stim (CD3/CD28 beads), and
681 AF conditioned media on Treg (**E**) proliferation, (**F**) ST2^{+}KLRG1^{+} expression, and (**G**)
682 Treg viability. **H**, Graphical illustration of IL-33 injection timeline in Foxp3^{creERT2}; ST2^{GFP}
683 mice to sort out type 2 Tregs. **I-J**, Quantitation comparing the effects of a combination of
684 AFs and stim on ST2^{+} and ST2^{-} Treg (**I**) proliferation and (**J**) ST2^{+}KLRG1^{+} expression. **K**,
685 Graphical illustration of infection timeline in Foxp3^{creERT2}; Tbet^{ZsGreen} mice to sort out type
686 1 Tregs. **L-M**, Quantitation comparing the effects of a combination of AFs and stim on
687 Tbet^{+} and Tbet^{-} Treg (**L**) proliferation and (**M**) viability. **N**, Heatmap illustrating markers
688 associated with AFs and fibrotic fibroblasts across a dose titration of TGFβ treatment. **O-**
689 **P**, Quantitation comparing effects of AFs and TGFβ-treated AFs on Treg (**O**) viability and
690 (**P**) proliferation. **Q**, Graphical illustration of the interactions between AFs and TGFβ-
691 treated AFs on type 2 and type 1 Tregs. Graphs show mean±s.d. ns = not significant,
692 *p<0.05, **p<0.01, ***p<0.001, ****p<0.0001; one-way ANOVA, Tukey post-test (**E-G, O-**
693 **P**); two-way ANOVA, Sidak's post-test (**I-J**, and **L-M**).
694
695 *Figure S5:*
696 **A**, Quantitation comparing effects of AFs and AlvFs on Treg proliferation. **B-D**,
697 Quantitation looking at effect of transwell cultures of AFs on Treg (**B**) proliferation, (**C**)
698 viability, and (**D**) ST2^{+}KLRG1^{+} expression. **E**, Quantitation looking at the effect of MHC II^{-}
699 $^{/-}$ AFs on Treg ST2^{+}KLRG1^{+} expression. **F-I**, (**F**) graphical illustration showing timeline of
700 IL-33 and AF treatment and their effects on Treg (**G**) proliferation, (**H**) ST2^{+}KLRG1^{+}
701 expression, and (**I**) viability. **J-K**, Quantitation of effect of IL-33$^{-/-}$ AFs on Treg (**J**)
702 proliferation and (**K**) ST2^{+} KLRG1^{+} expression. **L-M**, Quantitation comparing AF support
703 on effector (CD44^{+}) and naïve (CD62L^{+}) Treg (**L**) proliferation and (**M**) ST2^{+}KLRG1^{+}
704 expression. **N**, Quantitation comparing the effects of a combination of AFs and stim on

705 ST2$^+$ and ST2$^-$ Treg viability. **O**, Heatmap of control AFs or AFs cultured with IL-1β
706 illustrating markers associated with inflammatory fibroblasts. **P**, Volcano plot comparing
707 DEGs of control and IL-1β-treated AFs (10ng/mL). **Q-R**, Volcano plots comparing DEGs
708 of control and TGFβ-treated AFs (10ng/mL), looking at (**Q**) immune and (**R**) fibrosis
709 markers. **S**, Quantitation comparing effects of AFs and TGFβ-treated AFs on Treg
710 ST2$^+$KLRG1$^+$ expression. Graphs show mean±s.d. ns = not significant, *p<0.05,
711 **p<0.01, ***p<0.001, ****p<0.0001; one-way ANOVA, Tukey post-test (**A-E, G-K, S**);
712 two-way ANOVA, Sidak's post-test (**L-N**).
713
714
715 *Figure 6:*
716 **A**, Graphical illustration showing timeline of tamoxifen injections in T2 Treg deleter mice.
717 **B**, Graph showing differences in Gata3 MFI between control and T2 Treg deleter mice.
718 **C**, Quantitation showing differences in Gata3 MFI across Tregs, CD4 effector cells, and
719 ILC2s. **D**, Quantitation measuring frequency and numbers of ST2$^+$ Tregs between control
720 and flox mice. **E**, Quantitation measuring frequency and numbers of ST2$^+$KLRG1$^+$ Tregs
721 between control and flox mice. **F**, Representative FACS plots illustrating ST2 and KLRG1
722 expression in Tregs and CD4$^+$ T cells in control and T2 Treg deleter mice. **G-H**,
723 Quantitation at 3, 7, and 14 dpi showing continuous loss of ST2 expression in both (**G**)
724 frequency and (**H**) numbers in Tregs. **I-J**, Time course graphs illustrating exacerbated (**I**)
725 peripheral blood oxygen and (**J**) body weights in flox mice. Graphs show mean±s.d.
726 *p<0.05, **p<0.01, ***p<0.001, ****p<0.0001; one-way ANOVA, Tukey post-test (**C**).
727 Student's T-test (**D-E, G-H** (for each time point)). Mixed-effect analysis with Geisser-
728 Greenhouse correction (**I-J**).
729
730 *Figure S6:*
731 **A-C**, Quantitation showing frequency (left panels) and numbers (right panels) of tissue
732 resident (i.v.$^-$) (**A**) Tregs, (**B**) CD4$^+$ T cells, and (**C**) CD8$^+$ T cells. **D-E**, Quantitation
733 showing frequencies of (**D**) T2L and T1L Tregs and (**E**) T2L and T1L CD4$^+$ T cells. **F-N**,
734 Time course showing frequency and numbers of various immune cell populations
735 between control and flox mice at 3, 7, and 14 dpi. (**F, H, J, M, L**) Frequency of total CD45$^+$
736 cells of (**F**) CD8 T and B cells, (**H**) ILC2s and γδ T cells, (**J**) Neutrophils and NK cells, (**M**)
737 monocytes and macrophages, and (**L**) Eosinophils and alveolar macrophages. (**G, I, K,**
738 **O, N**) Numbers of (**G**) CD8 T and B cells, (**I**) ILC2s and γδ T cells, (**K**) Neutrophils and NK
739 cells, (**O**) monocytes and macrophages, and (**N**) Eosinophils and alveolar macrophages.
740 **P**, Graphical illustration showing Type 2-like Treg dynamics in control, TGFbfr2 cKO, and
741 T2 Treg deleter models. Graphs show mean±s.d. ns = no significance; Student's T-test
742 (**A-C**).

743 **Methods**

744

745 **Mice**

746

747 To trace regulatory T cells (Tregs), we used Foxp3^{eGFPcreERT2} mice (JAX: 016961)
748 intercrossed with Rosa26^{tdRFP} (JAX: 038164), which carry an allele encoding a robust
749 tandem-dimer RFP. These Foxp3^{creERT2}; Rosa26^{RFP} mice show RFP expression in *Foxp3*-
750 lineage cells upon tamoxifen administration. Foxp3^{creERT2}; Rosa26^{RFP} mice were further
751 crossed with an Il1r1^{eGFP} mouse line (generated by Anna Molofsky lab, UCSF), a Rorc^{eGFP}
752 BAC transgene knock-in mouse line (MGI: 3829387), and a Tbx21^{ZsGreen} transgenic
753 mouse line (generously provided by JinFang Zhu, Lab of Immune System Biology, NIH).
754 For our co-culture experiments and Treg isolation, we used Foxp3^{eGFP} reporter mice (JAX:
755 006772). Foxp3^{creERT2}; Rosa26^{RFP} mice were crossed with Gata3^{flox} mice (JAX: 028103)
756 to specifically delete *Gata3* expression from *Foxp3*-lineage cells upon tamoxifen
757 administration. Foxp3^{creERT2}; Rosa26^{RFP} mice were crossed to a PDGFRa^{GFP} knock-in
758 knock-out mouse line (JAX: 007669), and used as heterozygotes, to visualize relative
759 localization of Tregs to fibroblasts. To lineage trade sensory neurons, Nav1.8^{cre};
760 tdTomato$^{f/+}$ were used (generously provided by Sebastien Talbot, Department of
761 Biological Sciences, Queens University).

762

763 To conditionally delete fibroblast *Tgfbr2*, Col1a2creERT2 mice were intercrossed with
764 Tgfbr2$^{f/f}$ mice (both Tgfbr2-exon2flox, MGI 2384513, and Tgfbr2-exon4flox, Jackson
765 012603). To conditionally delete adventitial fibroblasts, Gli1^{creERT2} (JAX: 007913) mice
766 were crossed with Rosa26^{DTR} mice (JAX: 007900). To lineage trace profibrotic fibroblasts,
767 we crossed Cthrc1^{CreER} (generously provided by Dean Sheppard lab, UCSF) to
768 Rosa26$^{CAG\text{-}RFP}$ (JAX: 007914). For the above conditional knockout strains, controls were
769 littermate Cre-negative or flox-heterozygous mice.

770

771 The Saa3^{creER} mouse strain was generously provided by Tatsuya Tukui (Dean Sheppard
772 lab, UCSF) and generated by homology-directed repair at the endogenous Saa3 locus
773 using CRISPR–Cas9 endonuclease activity in C57BL/6 mice as described previously[18].
774 In brief, CRISPR RNA (crRNA) with input sequence GTAGTTGCTCCTCTTCTCGG and
775 trans-activating CRISPR RNA (tracrRNA) were obtained from IDT. A 5′ homology arm
776 was amplified from C57BL/6 mouse genomic DNA with forward primer 5′-
777 AGGTGAAATCTGTAGGTCAAAGATG-3′ and reverse primer 5′-
778 GTATCTTTTAGGCAGGCCAGCAGGT-3′. A 3′ homology arm was amplified with forward
779 primer 5′-GTTGTTCCCAGTCATGCTGC*TTC* CCGAGAAGAGGAGCAACTACTGGGT-
780 3′ (*protospacer adjacent motif (PAM) sequence CCC was altered to TTC) and reverse
781 primer 5′- GCAAAATTAGGGACCAATGACCTACTC-3′. A targeting vector with P2A-
782 creERT2 sequence flanked by 5′ and 3′ homology arms was generated using NEBuilder

783 HiFi DNA Assembly (NEB) and cloned into a pKO2 backbone plasmid. The targeting
784 vector was linearized at SalI (NEB) and NotI (NEB) sites flanking the donor DNA
785 sequence and the linearized donor DNA was purified by agarose gel electrophoresis with
786 GeneJet Gel Extraction kit (Thermo Fisher). Linearized donor DNA and CRISPR–Cas9
787 complex were injected into C57BL/6 fertilized zygotes, which were then implanted into
788 the oviducts of pseudopregnant female mice. A total of 195 embryos were implanted and
789 15 pups were born. Two founders were identified by genotyping. We used one founder to
790 expand the colony.

791 Mice were mixed-sex, backcrossed onto C57BL/6 for at least 10 generations. If not
792 otherwise stated, all experiments were performed with 8–16-week-old male and female
793 mice. All mice were bred and maintained in specific-pathogen-free conditions at the
794 animal facilities of UCSF and were used in accordance with institutional guidelines and
795 under study protocols approved by the UCSF Institutional Animal Care and Use
796 Committee.

797 **Tamoxifen-induced Cre recombination**

798 Mice were injected intraperitoneal (i.p.) with 200mL of tamoxifen (Sigma-Aldrich)
799 dissolved in corn oil at 10mg/mL.

800 **Influenza A (PR8) infection**

801 Influenza A/Puerto Rico 8/1934 (PR8) H1N1 strain was obtained from ATCC (VR-95),
802 aliquoted and stored in liquid nitrogen. Mice were anesthetized by i.p. injection with
803 ketamine–xylazine (Patterson Veterinary) or isoflurane and intranasally infected with ~60
804 plaque-forming units for each experiment. Mice were sacrificed at the indicated time
805 points and tissues were harvested and analyzed.

806 **qPCR analysis**

807 Lung lobes taken for qPCR were snap-frozen at -20°C in 1.5mL Eppendorf tubes. Lobes
808 were then homogenized in 600mL of buffer RLT (RNeasy Mini Kit, Benchmark D1032-
809 30) with a Precellys Evolution Touch Homogenizer (Bertin Technologies). Lysates were
810 then used to extract RNA according to the manufacturer's protocol of the RNeasy Mini
811 Kit. Eluted RNA was then converted to cDNA using SuperScript III First Strand Synthesis
812 System (Invitrogen). qPCR was run on a StepOnePlus Real-Time PCR system (Applied
813 Biosystems).

814 Primers used: NP-1 (5'-CAGCCTAATCAGACCAAATG-3' (forward) and 5'-
815 TACCTGCTTCTCAGTTCAAG-3' (reverse)),

816 **Tissue processing: Thick section imaging**

817 Following CO_2 euthanasia, mice were transcardially perfused with 10mL of DPBS and, if
818 not used for flow cytometry, flushed intra-tracheally with 4% PFA (Thermo Scientific).
819 Lung lobes were then stored in 4% PFA for 1-3 days at 4°C followed by cryoprotection
820 (30% sucrose). Lobes were frozen in O.C.T. (Thermo Scientific) on dry ice and sliced into
821 300mM sections on a cryostat (Leica). Sections were then placed into PBS to wash and
822 blocked (DPBS, 1% BSA, 0.3% TritonX-100, 1% mouse serum) overnight at 4°C.
823 Sections were then incubated in the primary antibody diluted in blocking buffer for 3 days
824 at 4°C. Sections are then washed with washing buffer (DPBS, 0.3% TritonX-100, 0.5% 1-
825 Thioglycerol) for three 30-minute washes at 37°C. Sections were then incubated
826 overnight at 4 °C with a secondary antibody solution diluted in blocking buffer. Sections
827 were washed once again for three 30-minute washes and then cleared using Ce3D
828 clearing solution (for 5mL: 2.75mL of 40% N-methylacetamide, 80% weight/volume
829 Histodenz, 5mL of TritonX-100, 25mL of thioglycerol) for one hour at room temperature.
830 Sections were then mounted and imaged with a Leica SP8 confocal microscope.

831 **Imaging Antibodies:**

832 Primary antibodies used for murine imaging include chicken anti-GFP (Aves Labs GFP-
833 1020, 1:200), rabbit anti-dsRed (Takara 632496, 1:300), rat anti-ER-TR7 (Novus
834 Biologicals NG100-64932), goat anti-Pi16 (R&D Systems AF4929), rabbit anti-proSP-C
835 (Millipore AB3786), goat anti-IL-33 (R&D Systems AF3626), and rat anti-EpCAM (BD
836 Pharmingen 552370).

837 Directly conjugated antibodies were also used including mouse anti-αSMA AF488
838 (eBioscience 53-9760-82), anti-αSMA AF405 (R&D Systems IC1420V025), rat anti-CD45
839 BV421 (BioLegend 103134), rat anti Lyve1 ef660 (eBioscience 50-0443-82) and rat anti-
840 CD45 (BioLegend 103124).

841 Secondary antibodies were used as necessary at protocol-specific concentrations,
842 conjugated to AF488, AF555, AF594, and AF647 (Life Technologies, Thermo-Fisher).

843 **Confocal microscopy**

844 Confocal images (for thick sections and quantification) were acquired using a Leica SP8
845 laser scanning confocal microscope equipped with an AOBS tunable detection pathway,
846 a white-light laser that excites between 470-670 nanometers, and a lighting deconvolution
847 module. An Apo IMM (H_2O Dipping) 20x 1.95mm working distance objective was used. Z
848 steps were acquired every 2.5 or 5uM.

849 **Image Analysis/Quantification**

850 Z-stacks were rendered in 3D and quantitatively analyzed using Bitplane Imaris v9.8
851 software package (Andor Technology OLC, Belfast, N. Ireland). Individual cells (e.g.,
852 lymphocytes) were annotated using the Imaris surface function based on fluorescent
853 reporter signal (e.g., Rosa26^{RFP}) when available, along with DAPI staining, and
854 size/morphological characteristics, with background signal in unrelated channels
855 excluded. 3D reconstructions of vessels and airways were generated using the Imaris
856 surface function based on fluorescent αSMA signal. 3D distances between Tregs and
857 αSMA surfaces were calculated using the Imaris Distance Transform Matlab extension.
858 Treg quantifications and distance calculations were performed across various lung slices,
859 prioritizing regions balanced between adventitial and alveolar regions. Similar surfacing
860 thresholds were applied across slices, and experiments for given cell types and
861 structures, and individual thresholds were adjusted when necessary to account for
862 varying tissue background. Damage patches were quantified by manually drawing
863 surfaces based on a combination of pro-SPC and CD45 fluorescent signal. Another
864 surface would then be drawn for the full lung slice, and a percentage was calculated by
865 dividing the volume of the damage patch by the volume of the whole lung.

866 **Tissue processing: single cell isolation (murine)**

867 Single-cell tissues were prepared from tissues including lung, spleen, and draining lymph
868 nodes (dLN). Immediately following CO_2 euthanasia, spleens were removed and put into
869 1X DPBS. Mice were subsequently transcardially perfused through the left ventricle with
870 10mL of DPBS. Lungs were then removed, as well as the mediastinal lymph nodes, and
871 put into DPBS. Spleen and lymph nodes were crushed through 70mM filters using 3mL
872 syringes and washed with FACS buffer (3% FBS, 0.5% NaN_3). Lungs were put into
873 gentleMACS tubes (Miltenyi Biotec 130-096-334) with 5mL of digestion media (40mg/mL
874 LiberaseTM and 80mg/mL of DNase I (Roche) in HBSS). Tubes were then placed on a
875 gentleMACS Octo Dissociator (Miltenyi Biotec 130-096-427) and spun. Tubes were then
876 placed at 37°C for 30 minutes and spun once more on the gentleMACS Octo Dissociator.
877 Digested tissue was subsequently filtered through 70 µm filters using 3mL syringes and
878 washed with FACS buffer. After filtration, samples are centrifuged at 1500rpm for 5
879 minutes at 4°C and resuspended in 1mL of 1X Pharmlyse buffer (BD Biosciences 555899)
880 for 2 minutes at 4°C (spleen and dLN skip the Pharmlyse step). Samples are then
881 quenched with 6mL of FACS buffer and centrifuged once more at 1500rpm for 5 minutes
882 at 4°C. Samples are then resuspended to the necessary concentration for staining.

883 **Flow cytometry**

884 Resuspended samples were stained in 96-well V-bottom plates. Surface staining was
885 performed at 4°C for 45 minutes in 50mL staining volume. For experiments involving
886 intracellular staining, cells were fixed and permeabilized using Foxp3 Transcription Factor

887 Staining Buffer Set (eBioscience) followed by staining at 4°C for 1 hour or overnight in
888 50mL staining volume. All samples were acquired on a BD LSRII Fortessa Dual or a BD
889 FACSAria II for cell sorting. Live cells were gated based on their forward and side scatter
890 followed by Zombie NIR fixable (BioLegend 423106), Fixable Viability Dye eF780
891 (eBioScience 65086514), Draq7 (Biolegend 424991), or DAPI (40,6-diamidine-20-
892 phenylindole dihydrochloride; Millipore Sigma D9542-10MG) exclusion. Lineages were
893 subsequently identified as follows:

894 T cells were identified as CD45+, CD11b-, CD19-, NK1.1-, CD3e+, CD4+ (CD4 T cells),
895 CD8a+ (CD8 T cells), Foxp3^{+} (Tregs), and were further defined as CD44^{-}CD62L+ (naïve
896 T cells), CD62L-, CD44+ (activated T cells), or CTV diluted (proliferating T cells).
897 Additionally, CD4 T cells and Tregs were defined as T-bet+ (Th1 T cells), Gata3+ or ST2^{+}
898 (Th2 T cells), or RORgt+ (Th17 T cells). Neutrophils were defined as CD45+, CD11b+,
899 Ly6G+ (and optionally Thy1-, CD19-, NK1.1-). Monocytes were defined as CD45+,
900 CD11b+, Ly6G-, Ly6C+ (and optionally Thy1-, CD19- , NK1.1-, Siglec F-). Macrophages
901 were defined as CD45+, Ly6G-, Ly6C-, CD64+ (optionally MERTK+). cDCs were
902 identified as CD45+, Ly6G-, Ly6C-, CD64-, MHCII+, CD11c+, and were further defined
903 as cDC1s (CD11b^{lo}, optionally SIRPa-) or cDC2s (CD11b^{hi}, optionally SIRPa+). B cells
904 were defined as CD45+, Thy1-, CD19+. Eosinophils were defined as CD45+, Thy1-,
905 CD19-, NK1.1-, Ly6G-, CD11b+, Siglec F+. Populations were backgated to verify purity
906 and gating.

907 Data were analyzed using FlowJo (Treestar, USA) and compiled in Prism (GraphPad)
908 software. Cell counts were performed using flow cytometry counting beads (CountBright
909 Absolute; Life Technologies) according to the manufacturer's instructions.

910 **Flow Cytometry Antibodies**

911 Antibodies used for flow cytometry include anti-CD45 (30-F11, BD Biosciences 564279),
912 anti-CD90.2 (Thy1, 53-2.1, Biolegend 140327, BD Biosciences 553004), anti-CD11b
913 (M1/70, Biolegend 101224 or BD Biosciences 563015), anti-CD19 (6D5, Biolegend
914 115554), anti-NK1.1 (PK136, Biolegend 108736), anti-CD3e (17A2, Biolegend 100216),
915 anti-CD4 (RM4-5, Biolegend 100557, or GK1.5, BD Biosciences 563050), anti-CD8a (53-
916 6.7, Biolegend 100750), anti-CD44 (IM7, Biolegend 103030), anti-CD69 (H1.2F3,
917 Biolegend 104505), anti-CD62L (MEL-14, Biolegend 104407), anti-Tbet (4B10, Biolegend
918 25-5825-80), anti-Gata3 (TWAJ, eBioscience 12- 9966-41), anti-RORgt (B2D,
919 eBioscience 17-6981-82), anti-Ly6G (1A8, Biolegend 127624), anti-Ly6C (HK1.4,
920 Biolegend 128011 or 128035), anti-CD64 (X-54-5/7.1, Biolegend 139323 or BD
921 Biosciences 558539), anti-MERTK (DS5MMER, eBioscience 46-5751-80), anti CD11c
922 (N418, Biolegend 117339 or 117318), anti-CD172a (SIRPa, P84, eBioscience 12-1721-
923 80), anti-Siglec-F (E50-2440, BD Biosciences 740956), anti-I-A/I-E (MHCII, M5/114.15.2,

924 BD Biosciences 748845), anti-CD192 (CCR2, 475301, BD Biosciences 747964), anti-
925 Foxp3 (FJK-16S, Invitrogen 53-5773-82), anti-gdTCR (GL3, Invitrogen 14-5711-82), anti-
926 CD25 (PC61, BioLegend 102030), anti-ST2 (DJ8, MD BioProducts 101001PE), anti-
927 CD152 (CTLA-4, UC10-4B9, BioLegend 106310), anti-KLRG1 (MAFA, BioLegend
928 138421), anit-CD278 (ICOS, C39A.4A, BioLegend 313537), anti-CD279 (PD-1,
929 29F.1A12, BioLegend 135225), anti-Ki67 (B56, BD Biosciences 564071), anti-podoplanin
930 (gp38, 8.1.1, BioLegend 127411), anti-PDGFRa (APA5, BioLegend 135908), anti-CD326
931 (EpCAM, G8.8 BioLegend 118320), biotinylated anti-CD31 (390, BioLegend 102404),
932 biotinylated anti-CD45 (30-F11, BioLegend 103104), and anti-Ly-6A (Sca-1, D7,
933 BioLegend 108131).

934 **Ex vivo co-culture**

935 For *ex vivo* co-culture experiments, lung adventitial fibroblasts (AFs) were obtained by
936 dissection as described above but using a different digest media. The digest media per
937 mouse was instead: 5mL 1X Dispase II, 112.5 U/mL Collagenase I, and 40ug/mL DNase
938 I. After cardiac perfusion, 1.5mL of digest media was injected through the trachea to
939 expand the lungs. Lungs were then chopped manually with sterile razors to small chunks
940 and placed into digestion media at 37°C for 30 minutes. Samples were then pushed
941 through a sterile 70mM filter with a 3mL syringe and centrifuged at 1500rpm at 4°C for 5
942 minutes. Samples were resuspended in sterile Pharmlyse, placed on ice for 1 minute,
943 then quenched and centrifuged again. Samples were resuspended in sterile FACS buffer
944 at 1mL/lung added and incubated with 4mL/Lung of rat serum (Thermo Fisher 10710C)
945 on ice for 10 minutes. Biotinylated anti-CD45 and anti-CD31 are added at 4mL/mL of cells
946 and incubated for 30 minutes on ice. Biotinylated cells were subsequently removed by
947 using EasySep Magnetic Beads (Stem Cell), according to the manufacturer's instructions.
948 AFs were plated at 10,000 cells/well in a flat-bottom 96-well plate in AF media (DMEM,
949 10% FBS, 1X Glutamax, and 1% penicillin/streptomycin) and incubated at 37°C, 5% CO_2
950 for 7 days, where regulatory T cells were added.

951 To sort Tregs, T cells were isolated from the spleen and cervical/inguinal lymph nodes of
952 reporter mice using EasySep Magnetic Bead negative selection, and the cells were
953 subsequently stained for sorting. Tregs were labeled with 5mM CellTrace Violet in PBS
954 (Thermo Scientific) for 10 minutes, followed by washing with Treg media (RPMI, 10%
955 FBS, 1X Glutamax, 1% penicillin/streptomycin, 25mM HEPES, and 1X NEAA),
956 centrifugation, and resuspension. Tregs were plated at 10,000 cells/well in all conditions.
957 For all Treg wells, 1000IU of IL-2 was added to ensure healthy Treg populations. As a
958 positive control, anti-CD3/CD28 T-cell activating DynaBeads (Thermo Scientific) were
959 magnetically washed in 1mL DPBS and added at 3:1 bead:cell ratio. After 72 hours of co-
960 culture, wells were mixed by pipetting, and cells were transferred to a V-bottom plate. The

961 remaining cells were trypsinized for 10 minutes at 37°C, quenched, centrifuged, and
962 added to the previous cells. Cells were then centrifuged and stained for flow cytometry.

963 For AFs treated with TGFβ, on Day 3 post-plating, 100mL of media was removed and
964 100mL of media containing the relevant amount of TGFβ was added. On the day of Treg
965 addition, the TGFβ-treated media was completely removed, and wells were washed with
966 PBS before addition of Tregs. For IL-33-treated Tregs, IL-33 was added at the same time
967 as IL-2 into the Treg media in its relative amounts.

968 **Murine scRNAseq data processing**
969
970 Sequencing data were aligned to mouse genome mm10 with CellRanger version 7.1.0
971 (scRNAseq experiment 1; time course of global cells) or version 7.2.0 (scRNAseq
972 experiment 2; time course of stromal cells) (10x Genomics). Data was processed using
973 the Seurat R package, version 4.3.3 (experiment 1) or 5.1.1 (experiment 2). We excluded
974 cells with high mitochondrial gene expression and low or high UMI and feature counts,
975 using the bottom and top 2.5 percentiles as our cutoff. *SCTransform* function was
976 performed before clustering. Principle components were calculated using Seurat's
977 *RunPCA* function, followed by graph-based clustering using Seurat's *FindNeighbors*
978 (dims =1:30 for experiment 1, dims = 1:15 for experiment 2) and *FindClusters* (res = 0.25
979 for experiment 1, res = 0.8 for experiment 2) functions and 2D visualization using Seurat's
980 *RunUMAP* function (dims = 1:30 for experiment 1, dims = 1:15 for experiment 2). We
981 used a combination of *FeaturePlot*, *DotPlot,* and *VlnPlot* to identify cell clusters (for both
982 experiments) using common and well-validated lineage marker genes (e.g., *Col1a1,*
983 *Col1a2, Pdgfra* [fibroblasts]; *Pecam1* [endothelial]; *Itgam, Itgax* [myeloid]; *Cd3e, Cd4,*
984 *Cd8* [T cells]; *Sftpc* [epithelial]; *Scube2, Ces1d* [alveolar fibroblasts]; *Pi16, Ccl11, Col14a1*
985 [adventitial fibroblasts]; *Saa3, Ccl2, Ifitm3* [inflammatory fibroblasts]; *Pdgfrb, Cox4i2*
986 [pericytes]; *Acta2* [smooth muscle]; *Acta2, Hhip* [peribronchial], abd *Msln, Wt1*
987 [mesothelial]). We identified and excluded 2 clusters made up of likely doublets and
988 contaminants based on gene expression, visualizing resultant clusters on UMAPs and
989 dot plots using Seurat. Final datasets comprised 31,603 cells including 19,381
990 lymphocytes; 7472 myeloid cells; 2862 fibroblasts; 1712 endothelial cells; and 176
991 epithelial cells (experiment 1) and 34,995 cells including 18,793 alveolar fibroblasts;
992 11,886 adventitial fibroblasts; 1362 inflammatory fibroblasts; 1138 pericytes; 760 smooth
993 muscle cells; 553 peribronchial cells; 392 eptihelial cells; and 111 mesothelial cells
994 (experiment 2). Additional feature plots, UMAP plots and dot plots, and heatmaps were
995 generated using Seurat.
996
997 Fibroblasts and immune cells were subset and reclustered as above. In experiment 1,
998 Tregs were found by reclustering the lymphocyte population (dims = 1:15, res = 0.8) and
999 a combination of *FeaturePlot*, *DotPlot,* and *VlnPlot* to identify clusters high for *Foxp3*

expression. Clusters were isolated and reclustered again (dims = 1:10, res = 0.9) and a combination of *FeaturePlot*, *DotPlot,* and *VlnPlot* to identify clusters high for *Foxp3* expression was once again used and isolated for final downstream analysis. Fibroblasts were found by reclustering the fibroblast population (dims = 1:10, res = 0.8) and a combination of *FeaturePlot*, *DotPlot,* and *VlnPlot* to identify clusters high for canonical fibroblast markers. Clusters were isolated and reclustered again (1:10, res = 0.8) for downstream analysis. In experiment 2, adventitial fibroblasts were isolated and reclustered (dims = 1:15, res = 0.8) for downstream analysis. Clusters expressing high levels of myeloid or genes were excluded as likely contaminants and removed from global UMAP and bar plots. For experiment 2, in the adventitial fibroblast cluster, clusters of different AF states were found by using *AddModuleScore* (selecting for genes unique to each AF state such *Aqp1* and *Il33*) and violin plots. Relative abundance across time was calculated for each fibroblast subcluster after normalizing for timepoint or condition sample size (i.e., total # cells). Multi-gene scores were calculated as follows and generated using *AddModuleScore.* Profibrotic fibroblasts scores were calculated using a combination of the following genes: *Cthrc1, Acta2, Col1a1, Vim, Postn, Tnc, Lrrc15,* and *Spp1*. Type 2-like Treg scores were calculated using a combination of the following genes which are known to associate with type 2 immunity or type 2-like Tregs: *Gata3, Il1rl1, Areg, Prdm1, Il2ra, Irf4,* and *Setd2*[71,79]. Similarly, type 1-like Treg scores were calculated using a combination of the following genes: *Tbx21, Cxcr3, Ifng, Cx3cr1, Il10,* and *Tgfb1*. Finally, AF immune-functionality scores were calculated using a combination of markers seen to be unique to immune-modulatory AFs: *Il33, Ptgs2, Lum,* and *Ccl11*.

Xenium spatial transcriptomics

A custom-designed 480 gene stromal-immune panel (Table somewhere) was generated using insights from single cell studies (see sc refs in paper, Anthony's and Dean Sheppard's). Following CO2 euthanasia, mice were transcardially perfused with 10mL of D-PBS and lung lobes were collected. Tissues were immediately fixed in 4% PFA and left to fix for 24h at 4C. Samples were washed 3x times with 1x D-PBS before transfer to 70% Ethanol and FFPE blocks were made (using UCSF Gladstone histology core, need to cite). Once blocks were generated, we partnered with UCSF Genomics CoLabs(citation) to process and analyze samples. In brief, FFPE blocks were sectioned using a microtome at 10-µm thickness, placed on Xenium slides, deparaffinized and de-crosslinked according to manufacturer instructions (CG000578, Rev F, 10x Genomics). Probes were hybridized, ligated, and amplified on slide, cell segmentation staining and amplification quenching were performed (CG000749, Rev B, 10x Genomics) and slides were analyzed with a Xenium Analyzer (CG000584, 10X Genomics). After scanning, slides were removed from the analyzer and subjected to post-run H&E per 10x Genomics protocol (CG000613, Rev B, 10x Genomics).

Raw Xenium Data was loaded into RStudio as a Seurat object using *LoadXenium* function. Cells with <10 counts, <5 features or the top 2% of outliers in either metric were excluded per slide. Following exclusion Seurat objects were merged into a single dataset and log-normalized using Seurat's *NormalizeData* function, variable features were identified, and *ScaleData* function was applied. Principle components were calculated using Seurat's *RunPCA* function, followed by graph-based clustering with Seurat's *FindNeighbors* (dims 1:20 k.param = 16) and *FindClusters*(res = 0.5) functions. Finally, data was visualized in 2D with Seurat's RunUMAP function (dims 1:20) and *JoinLayers* was run. To aid in cell type identification, we used *FindAllMarkers* to identify cluster-defining DEGs. Further cell-identification workflow follows as described in the scRNAseq data processing method. Clusters were spatially visualized using the 10x Xenium Explorer tool.

Acknowledgments

We thank Dr. Richard Locksley for his constructive feedback on this manuscript, as well as the UCSF Parnassus Flow Core RRID:SCR018206 and DRC Center Grant NIH P30 DK063720, the UCSF Biological Imaging and Development Core (BIDC), the UCSF Genomics CoLab, the UCSF Institute for Human Genetics, and Histowiz, Inc. for instruments and services. D.S. is supported by the NHLBI (NIH R01HL142568). A.B.M., and A.V.M. are supported by the NINDS (NIH R01NS126765), UCSF PBBR grant, and UCSF Dept. of Lab Medicine discretionary funds; A.B.M. is additionally supported by the NIAID (NIH R01AI162806).

Statistical analysis

All data were analyzed by comparison of means using unpaired (unless otherwise noted) two-tailed Student's t-tests; for multiple comparisons, one-way or two-way ANOVA (with Tukey or Sidak's post hoc test) was used as appropriate (Prism, GraphPad Software, La Jolla, CA). ns = not significant, *$p<0.05$, **$p<0.01$, ***$p<0.001$, ****$p<0.0001$. Figures display means ± standard deviation (SD) unless otherwise noted. When possible, results from independent experiments were pooled. All data points reflect individual biological mouse replicates (flow analysis) or individual tissue slices analyzed (imaging), unless otherwise noted. For imaging experiments, all analysis was performed with at least three mice from at least two independent experiments, with two or more fields analyzed per mouse.

References:

1. Zablockienė, B. *et al.* Zanamivir Diminishes Lung Damage in Influenza A Virus-infected Mice by Inhibiting Nitric Oxide Production. *In Vivo* **32**, 473–478 (2018).

1077 2. Bos, L. D. J. & Ware, L. B. Acute respiratory distress syndrome: causes, pathophysiology,
1078 and phenotypes. *The Lancet* **400**, 1145–1156 (2022).
1079 3. Short, K. R., Kroeze, E. J. B. V., Fouchier, R. A. M. & Kuiken, T. Pathogenesis of influenza-
1080 induced acute respiratory distress syndrome. *Lancet Infect. Dis.* **14**, 57–69 (2014).
1081 4. Diamond, M., Peniston, H. L., Sanghavi, D. K. & Mahapatra, S. Acute Respiratory Distress
1082 Syndrome. in *StatPearls [Internet]* (StatPearls Publishing, 2024).
1083 5. Wu, C. *et al.* Risk Factors Associated With Acute Respiratory Distress Syndrome and Death
1084 in Patients With Coronavirus Disease 2019 Pneumonia in Wuhan, China. *JAMA Intern. Med.*
1085 **180**, 1–11 (2020).
1086 6. Bal, A. *et al.* Influenza-induced acute respiratory distress syndrome during the 2010-2016
1087 seasons: bacterial co-infections and outcomes by virus type and subtype. *Clin. Microbiol.*
1088 *Infect.* **26**, 947.e1-947.e4 (2020).
1089 7. Zhang, P. *et al.* Long-term bone and lung consequences associated with hospital-acquired
1090 severe acute respiratory syndrome: a 15-year follow-up from a prospective cohort study.
1091 *Bone Res.* **8**, 8 (2020).
1092 8. Das, K. M. *et al.* Follow-up chest radiographic findings in patients with MERS-CoV after
1093 recovery. *Indian J. Radiol. Imaging* **27**, 342–349 (2017).
1094 9. Torres-Castro, R. *et al.* Respiratory function in patients post-infection by COVID-19: a
1095 systematic review and meta-analysis. *Pulmonology* **27**, 328–337 (2021).
1096 10. Gulati, A. & Lakhani, P. Interstitial lung abnormalities and pulmonary fibrosis in COVID-
1097 19 patients: a short-term follow-up case series. *Clin. Imaging* **77**, 180–186 (2021).
1098 11. Choi, E. S. *et al.* Enhanced monocyte chemoattractant protein-3/CC chemokine ligand-7
1099 in usual interstitial pneumonia. *Am. J. Respir. Crit. Care Med.* **170**, 508–515 (2004).
1100 12. Boyd, D. F. *et al.* Exuberant fibroblast activity compromises lung function via ADAMTS-
1101 4. *Nature* **587**, 466–471 (2020).

1102 13. TGFβ signalling in context | Nature Reviews Molecular Cell Biology.
1103 https://www.nature.com/articles/nrm3434.
1104 14. Skalli, O. *et al.* A monoclonal antibody against alpha-smooth muscle actin: a new probe
1105 for smooth muscle differentiation. *J. Cell Biol.* **103**, 2787–2796 (1986).
1106 15. Darby, I., Skalli, O. & Gabbiani, G. Alpha-smooth muscle actin is transiently expressed
1107 by myofibroblasts during experimental wound healing. *Lab. Investig. J. Tech. Methods*
1108 *Pathol.* **63**, 21–29 (1990).
1109 16. Rock, J. R. *et al.* Multiple stromal populations contribute to pulmonary fibrosis without
1110 evidence for epithelial to mesenchymal transition. *Proc. Natl. Acad. Sci. U. S. A.* **108**, E1475-
1111 1483 (2011).
1112 17. Tsukui, T. *et al.* Collagen-producing lung cell atlas identifies multiple subsets with distinct
1113 localization and relevance to fibrosis. *Nat. Commun.* **11**, 1920 (2020).
1114 18. Tsukui, T., Wolters, P. J. & Sheppard, D. Alveolar fibroblast lineage orchestrates lung
1115 inflammation and fibrosis. *Nature* **631**, 627–634 (2024).
1116 19. Djurec, M. *et al.* Saa3 is a key mediator of the protumorigenic properties of cancer-
1117 associated fibroblasts in pancreatic tumors. *Proc. Natl. Acad. Sci. U. S. A.* **115**, E1147–
1118 E1156 (2018).
1119 20. Ewing-Crystal, N. A. *et al.* Dynamic fibroblast–immune interactions shape recovery after
1120 brain injury. *Nature* 1–11 (2025) doi:10.1038/s41586-025-09449-2.
1121 21. Dahlgren, M. W. *et al.* Adventitial Stromal Cells Define Group 2 Innate Lymphoid Cell
1122 Tissue Niches. *Immunity* **50**, 707-722.e6 (2019).
1123 22. Buechler, M. B. *et al.* Cross-tissue organization of the fibroblast lineage. *Nature* **593**,
1124 575–579 (2021).
1125 23. McGowan, S. E. & Torday, J. S. The pulmonary lipofibroblast (lipid interstitial cell) and its
1126 contributions to alveolar development. *Annu. Rev. Physiol.* **59**, 43–62 (1997).

1127 24. Agha, E. E. *et al.* Two-Way Conversion between Lipogenic and Myogenic Fibroblastic
1128 Phenotypes Marks the Progression and Resolution of Lung Fibrosis. *Cell Stem Cell* **20**, 261-
1129 273.e3 (2017).
1130 25. PANG, G., COUCH, L., BATEY, R., CLANCY, R. & CRIPPS, A. GM-CSF, IL-1α, IL-β, IL-
1131 6, IL-8, IL-10, ICAM-1 and VCAM-1 gene expression and cytokine production in human
1132 duodenal fibroblasts stimulated with lipopolysaccharide, IL-1α and TNF-α. *Clin. Exp.*
1133 *Immunol.* **96**, 437–443 (1994).
1134 26. Salminen, A., Kaarniranta, K. & Kauppinen, A. Tissue fibroblasts are versatile immune
1135 regulators: An evaluation of their impact on the aging process. *Ageing Res. Rev.* **97**, 102296
1136 (2024).
1137 27. Wei, K., Nguyen, H. N. & Brenner, M. B. Fibroblast pathology in inflammatory diseases.
1138 *J. Clin. Invest.* **131**, e149538.
1139 28. Krishnamurty, A. T. *et al.* LRRC15+ myofibroblasts dictate the stromal setpoint to
1140 suppress tumour immunity. *Nature* **611**, 148–154 (2022).
1141 29. Powell, D. W. *et al.* Myofibroblasts. I. Paracrine cells important in health and disease.
1142 *Am. J. Physiol.-Cell Physiol.* **277**, C1–C19 (1999).
1143 30. Jovisic, M., Mambetsariev, N., Singer, B. D. & Morales-Nebreda, L. Differential roles of
1144 regulatory T cells in acute respiratory infections. *J. Clin. Invest.* **133**, (2023).
1145 31. Lin, S., Wu, H., Wang, C., Xiao, Z. & Xu, F. Regulatory T Cells and Acute Lung Injury:
1146 Cytokines, Uncontrolled Inflammation, and Therapeutic Implications. *Front. Immunol.* **9**, 1545
1147 (2018).
1148 32. Yang, A. Y. *et al.* Lung tissue-resident memory T cells optimize protection by IL-10
1149 regulation of innate immunity. *J. Exp. Med.* **223**, e20242307 (2026).
1150 33. Kaiser, K. A., Loffredo, L. F., Santos-Alexis, K. de L., Ringham, O. R. & Arpaia, N.
1151 Regulation of the alveolar regenerative niche by amphiregulin-producing regulatory T cells. *J.*
1152 *Exp. Med.* **220**, e20221462 (2023).

1153 34. Arpaia, N. *et al.* A Distinct Function of Regulatory T Cells in Tissue Protection. *Cell* **162**,
1154 1078–1089 (2015).
1155 35. Savage, T. M. *et al.* Amphiregulin from regulatory T cells promotes liver fibrosis and
1156 insulin resistance in non-alcoholic steatohepatitis. *Immunity* **57**, 303-318.e6 (2024).
1157 36. Wachtendorf, S. *et al.* The ST2+ Treg/amphiregulin axis protects from immune-mediated
1158 hepatitis. *Front. Immunol.* **15**, 1351405 (2024).
1159 37. Ehnold, L.-I. *et al.* Treg derived Amphiregulin protects from murine lupus nephritis via
1160 tissue reparative effects. *Sci. Rep.* **15**, 7776 (2025).
1161 38. Delacher, M. *et al.* Genome-wide DNA-methylation landscape defines specialization of
1162 regulatory T cells in tissues. *Nat. Immunol.* **18**, 1160–1172 (2017).
1163 39. Chang, S. K. *et al.* Stromal cell cadherin-11 regulates adipose tissue inflammation and
1164 diabetes. *J. Clin. Invest.* **127**, 3300–3312.
1165 40. Kolodin, D. *et al.* ANTIGEN- AND CYTOKINE-DRIVEN ACCUMULATION OF
1166 REGULATORY T CELLS IN VISCERAL ADIPOSE TISSUE OF LEAN MICE. *Cell Metab.* **21**,
1167 543–557 (2015).
1168 41. Kuswanto, W. *et al.* Poor repair of skeletal muscle in aging mice reflects a defect in local,
1169 interleukin-33-dependent, accumulation of regulatory T cells. *Immunity* **44**, 355–367 (2016).
1170 42. Chen, Z. *et al.* Fibroblast-derived alarmin promotes oral wound healing by activating
1171 regulatory T cells that relay pro-angiogenic and anti-inflammatory responses. *Cell Rep.* **45**,
1172 116829 (2026).
1173 43. Dahlgren, M. W. & Molofsky, A. B. Adventitial Cuffs: Regional Hubs for Tissue Immunity.
1174 *Trends Immunol.* **40**, 877–887 (2019).
1175 44. Doherty, D. F., Roets, L. & Krasnodembskaya, A. D. The Role of Lung Resident
1176 Mesenchymal Stromal Cells in the Pathogenesis and Repair of Chronic Lung Disease. *Stem*
1177 *Cells* **41**, 431–443 (2023).

1178 45. Ray, S. *et al.* Rare SOX2+ Airway Progenitor Cells Generate KRT5+ Cells that
1179 Repopulate Damaged Alveolar Parenchyma following Influenza Virus Infection. *Stem Cell*
1180 *Rep.* **7**, 817–825 (2016).
1181 46. Vaughan, A. E. *et al.* Lineage-negative progenitors mobilize to regenerate lung
1182 epithelium after major injury. *Nature* **517**, 621–625 (2015).
1183 47. Kathiriya, J. J. *et al.* Human alveolar type 2 epithelium transdifferentiates into
1184 metaplastic KRT5+ basal cells. *Nat. Cell Biol.* **24**, 10–23 (2022).
1185 48. Griffith, J. W. *et al.* Regulatory T cell-derived IL-1Ra suppresses the innate response to
1186 respiratory viral infection. *Nat. Immunol.* **24**, 2091–2107 (2023).
1187 49. Li, B. W. S. *et al.* T cells and ILC2s are major effector cells in influenza-induced
1188 exacerbation of allergic airway inflammation in mice. *Eur. J. Immunol.* **49**, 144–156 (2019).
1189 50. Monticelli, L. A. *et al.* Innate lymphoid cells promote lung tissue homeostasis following
1190 acute influenza virus infection. *Nat. Immunol.* **12**, 1045–1054 (2011).
1191 51. Califano, D. *et al.* IFN-γ increases susceptibility to influenza A infection through
1192 suppression of group II innate lymphoid cells. *Mucosal Immunol.* **11**, 209–219 (2018).
1193 52. Jung, H. *et al.* An ILC2–chitinase circuit restores lung homeostasis after epithelial injury.
1194 *Sci. Immunol.* **9**, eadl2986 (2024).
1195 53. Molofsky, A. B. *et al.* Interleukin-33 and Interferon-γ Counter-Regulate Group 2 Innate
1196 Lymphoid Cell Activation during Immune Perturbation. *Immunity* **43**, 161–174 (2015).
1197 54. Worrell, J. C. *et al.* Lung structural cells are altered by influenza virus leading to rapid
1198 immune protection following re-challenge. *Nat. Commun.* **16**, 7061 (2025).
1199 55. Khadim, A. *et al.* Myofibroblasts emerge during alveolar regeneration following influenza-
1200 virus-induced lung injury. *Cell Rep.* **44**, 115248 (2025).
1201 56. Tsukui, T. & Sheppard, D. Stromal heterogeneity in the adult lung delineated by single-
1202 cell genomics. *Am. J. Physiol.-Cell Physiol.* **328**, C1964–C1972 (2025).

1203 57. Compagnone, N. *et al.* Residual lung damage following ARDS in COVID-19 ICU
1204 survivors. *Acta Anaesthesiol. Scand.* **66**, 223–231 (2022).
1205 58. Huang, W. J. & Tang, X. X. Virus infection induced pulmonary fibrosis. *J. Transl. Med.*
1206 **19**, 496 (2021).
1207 59. BRINGARDNER, B. D., BARAN, C. P., EUBANK, T. D. & MARSH, CLAY. B. The Role
1208 of Inflammation in the Pathogenesis of Idiopathic Pulmonary Fibrosis. *Antioxid. Redox Signal.*
1209 **10**, 287–301 (2008).
1210 60. Camp, J. V. & Jonsson, C. B. A Role for Neutrophils in Viral Respiratory Disease. *Front.*
1211 *Immunol.* **8**, (2017).
1212 61. Tang, B. M. *et al.* Neutrophils-related host factors associated with severe disease and
1213 fatality in patients with influenza infection. *Nat. Commun.* **10**, 3422 (2019).
1214 62. Schultz-Cherry, S. Role of NK cells in influenza infection. *Curr. Top. Microbiol. Immunol.*
1215 **386**, 109–120 (2015).
1216 63. Boothby, I. C. *et al.* Early-life inflammation primes a T helper 2 cell–fibroblast niche in
1217 skin. *Nature* **599**, 667–672 (2021).
1218 64. Dahlgren, M. W. & Molofsky, A. B. Adventitial cuffs: regional hubs for tissue immunity.
1219 *Trends Immunol.* **40**, 877–887 (2019).
1220 65. Altieri, A. & Buechler, M. B. Adventitial fibroblast–ILC2 niche restrains liver fibrosis. *Nat.*
1221 *Rev. Immunol.* **23**, 477–477 (2023).
1222 66. Atakkatan, A. *et al.* Complement-producing adventitial fibroblasts form an IL-33 alarmin
1223 hub that maintains ILC2s during airway allergy. *Cell Rep.* **44**, (2025).
1224 67. Stockis, J. *et al.* Cross-talk between ILC2 and Gata3high Tregs locally constrains
1225 adaptive type 2 immunity. *Sci. Immunol.* **9**, eadl1903 (2024).
1226 68. Cautivo, K. M. *et al.* Interferon gamma constrains type 2 lymphocyte niche boundaries
1227 during mixed inflammation. *Immunity* **55**, 254-271.e7 (2022).

1228 69. D'Alessio, F. R. *et al.* CD4+CD25+Foxp3+ Tregs resolve experimental lung
1229 injury in mice and are present in humans with acute lung injury. *J. Clin. Invest.* **119**, 2898–
1230 2913 (2009).
1231 70. Chen, Z. *et al.* Fibroblast-derived alarmin promotes oral wound healing by activating
1232 regulatory T cells that relay pro-angiogenic and anti-inflammatory responses. *Cell Rep.* **45**,
1233 116829 (2026).
1234 71. Wohlfert, E. A. *et al.* GATA3 controls Foxp3^{+} regulatory T cell fate during inflammation in
1235 mice. *J. Clin. Invest.* **121**, 4503–4515 (2011).
1236 72. Zhang, Y. *et al.* CCL19-producing fibroblasts promote tertiary lymphoid structure
1237 formation enhancing anti-tumor IgG response in colorectal cancer liver metastasis. *Cancer*
1238 *Cell* **42**, 1370-1385.e9 (2024).
1239 73. Deng, Z. *et al.* TGF-β signaling in health, disease and therapeutics. *Signal Transduct.*
1240 *Target. Ther.* **9**, 61 (2024).
1241 74. Mu, D. *et al.* The integrin alpha(v)beta8 mediates epithelial homeostasis through MT1-
1242 MMP-dependent activation of TGF-beta1. *J. Cell Biol.* **157**, 493–507 (2002).
1243 75. Annes, J. P., Rifkin, D. B. & Munger, J. S. The integrin alphaVbeta6 binds and activates
1244 latent TGFbeta3. *FEBS Lett.* **511**, 65–68 (2002).
1245 76. Munger, J. S. *et al.* The integrin alpha v beta 6 binds and activates latent TGF beta 1: a
1246 mechanism for regulating pulmonary inflammation and fibrosis. *Cell* **96**, 319–328 (1999).
1247 77. Worthington, J. J. *et al.* Integrin αvβ8-Mediated TGF-β Activation by Effector Regulatory
1248 T Cells Is Essential for Suppression of T-Cell-Mediated Inflammation. *Immunity* **42**, 903–915
1249 (2015).
1250 78. Lainé, A. *et al.* Regulatory T cells promote cancer immune-escape through integrin
1251 αvβ8-mediated TGF-β activation. *Nat. Commun.* **12**, 6228 (2021).

79. Setd2 supports GATA3+ST2+ thymic-derived Treg cells and suppresses intestinal inflammation | Nature Communications. https://www.nature.com/articles/s41467-022-35250-0.

Figure 1

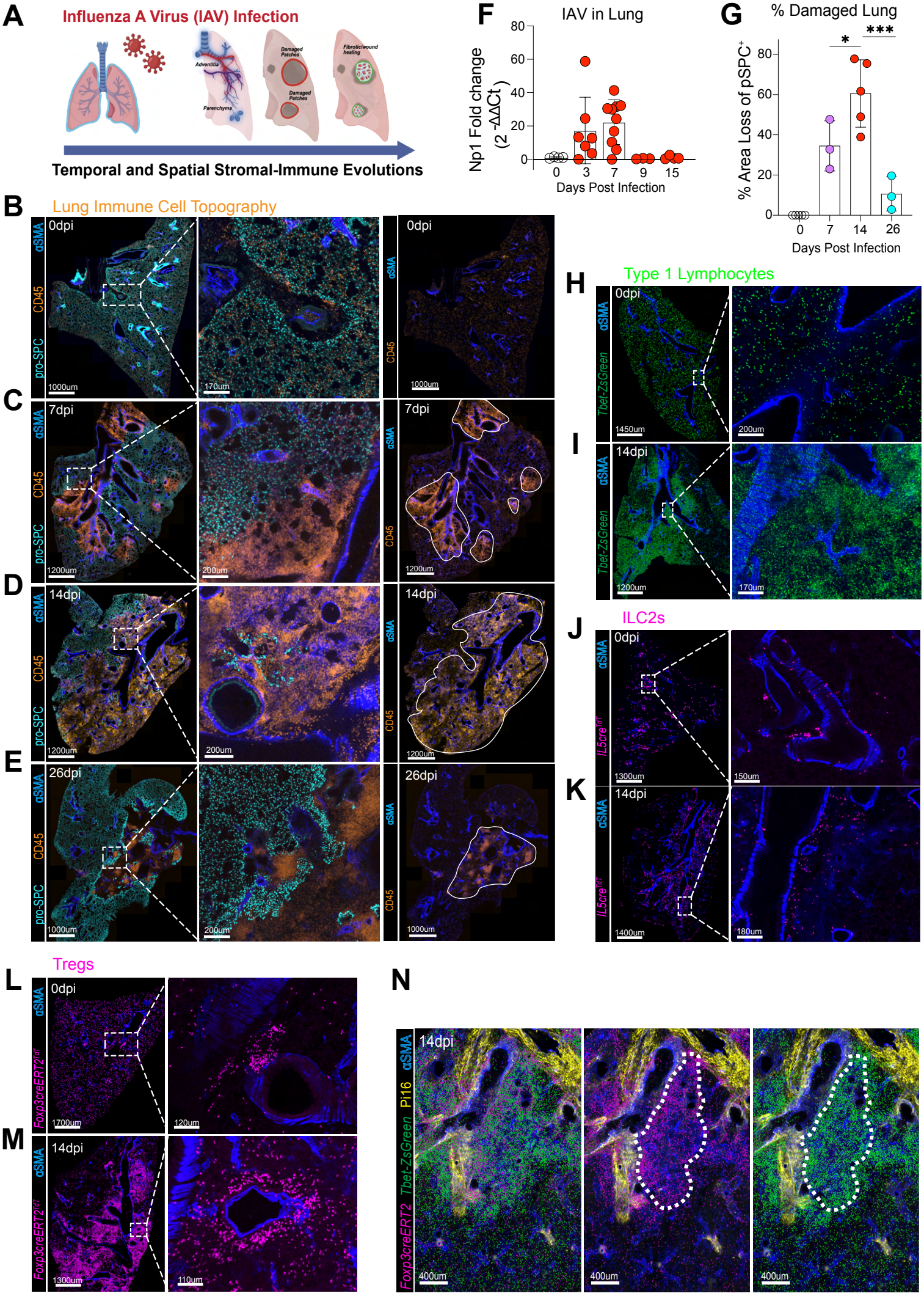
A
Influenza A Virus (IAV) Infection
Adventitia
Parenchyma
Damaged Patches
Damaged Patches
Fibrotic/wound healing
Temporal and Spatial Stromal-Immune Evolutions
F
IAV in Lung
Np1 Fold change (2 -ΔΔCt)
Days Post Infection
G
% Damaged Lung
% Area Loss of pSPC+
Days Post Infection
B
Lung Immune Cell Topography
C
D
E
αSMA
CD45
pro-SPC
0dpi
7dpi
14dpi
26dpi
1000um
170um
1200um
200um
1000um
H
Type 1 Lymphocytes
I
Tbet-ZsGreen
1450um
200um
1200um
170um
J
ILC2s
K
ILcre
1300um
150um
1400um
180um
L
Tregs
M
Foxp3creERT2
1700um
120um
1300um
110um
N
Foxp3creERT2 Tbet-ZsGreen Pi16 αSMA
400um

Figure S1

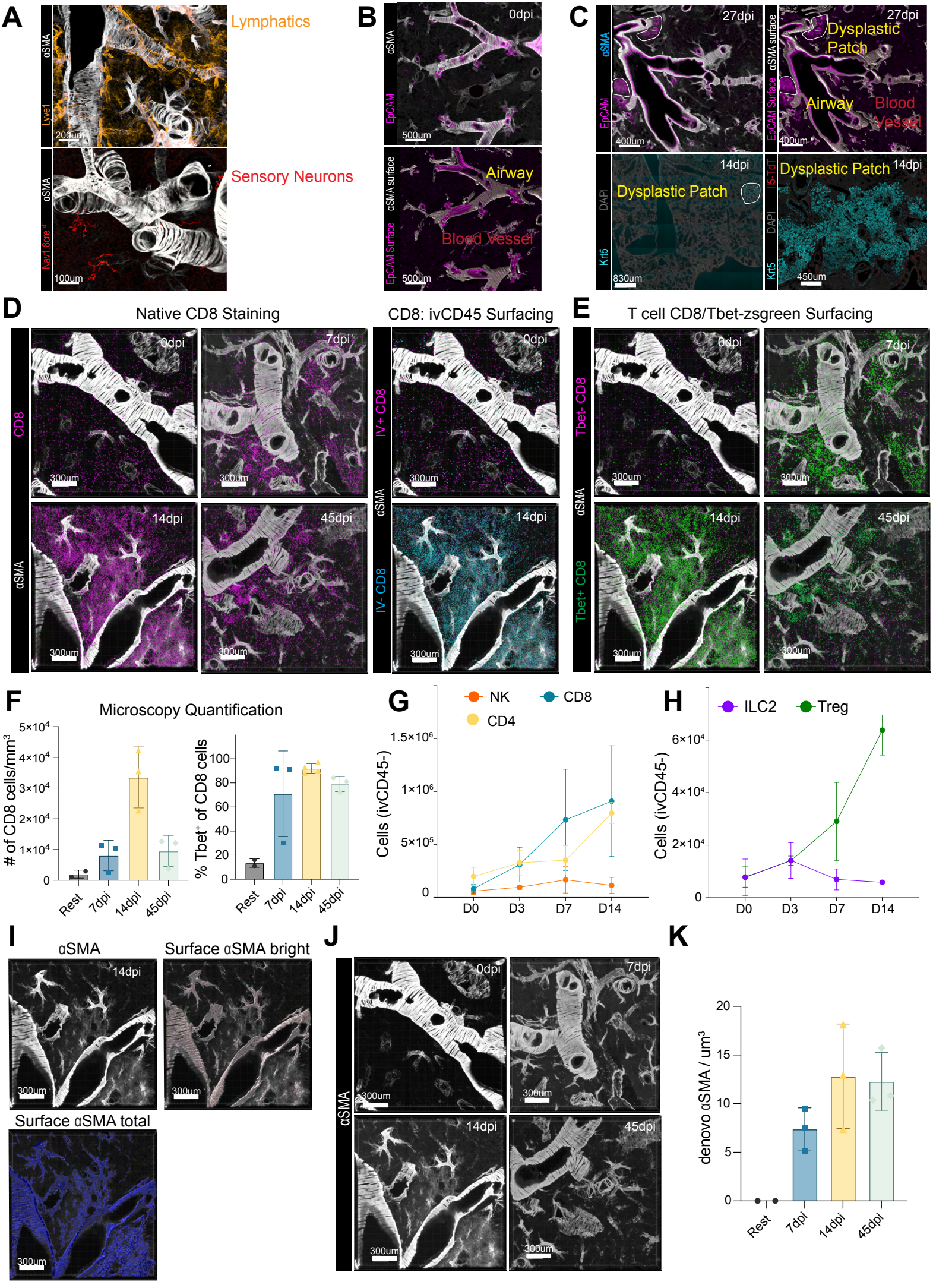
A
αSMA
Lyve1
200um
Lymphatics
αSMA
Nav1.8cre(d)
100um
Sensory Neurons
B
αSMA
EpCAM
0dpi
500um
αSMA surface
EpCAM Surface
Airway
Blood Vessel
500um
C
αSMA
EpCAM
27dpi
400um
αSMA surface
EpCAM Surface
Dysplastic Patch
Airway
Blood Vessel
DAPI
Krt5
14dpi
Dysplastic Patch
830um
Il5-TdT
450um
D
Native CD8 Staining
CD8: ivCD45 Surfacing
CD8
αSMA
IV+ CD8
IV- CD8
0dpi
7dpi
14dpi
45dpi
300um
E
T cell CD8/Tbet-zsgreen Surfacing
Tbet- CD8
Tbet+ CD8
F
Microscopy Quantification
# of CD8 cells/mm³
% Tbet⁺ of CD8 cells
Rest
7dpi
14dpi
45dpi
G
NK
CD8
CD4
Cells (ivCD45-)
D0
D3
D7
D14
H
ILC2
Treg
I
αSMA
Surface αSMA bright
Surface αSMA total
J
K
denovo αSMA / um³

Figure 2

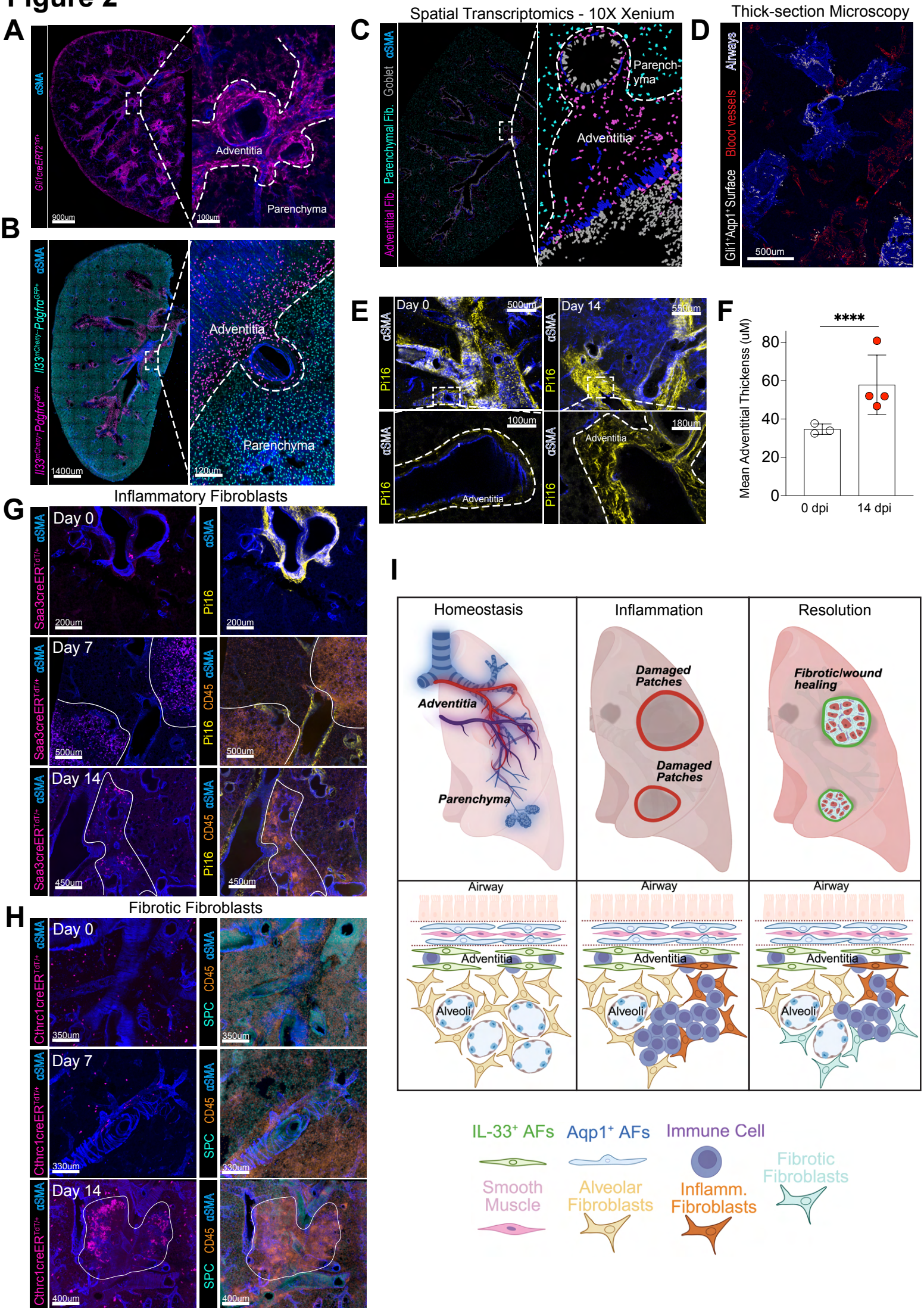
A
αSMA
Gli1creERT2cre+
Adventitia
Parenchyma
900um
100um
B
αSMA
Il33mCherry+Pdgfrα GFP+
Il33mCherry+Pdgfrα GFP+
Adventitia
Parenchyma
1400um
120um
Spatial Transcriptomics - 10X Xenium
C
αSMA
Goblet
Parenchymal Fib.
Adventitial Fib.
Parenchyma
Adventitia
Thick-section Microscopy
D
Airways
Blood vessels
Gli1+Aqp1+ Surface
500um
E
Day 0
Day 14
αSMA
Pi16
500um
550um
100um
180um
Adventitia
F
****
Mean Adventitial Thickenss (uM)
80
60
40
20
0
0 dpi
14 dpi
G
Inflammatory Fibroblasts
Saa3creERTdT/+
Day 0
Day 7
Day 14
αSMA
Pi16
CD45
200um
500um
450um
H
Fibrotic Fibroblasts
Cthrc1creERTdT/+
SPC
350um
330um
400um
I
Homeostasis
Inflammation
Resolution
Adventitia
Parenchyma
Damaged Patches
Fibrotic/wound healing
Airway
Alveoli
IL-33+ AFs
Aqp1+ AFs
Immune Cell
Smooth Muscle
Alveolar Fibroblasts
Inflamm. Fibroblasts
Fibrotic Fibroblasts

Figure S2

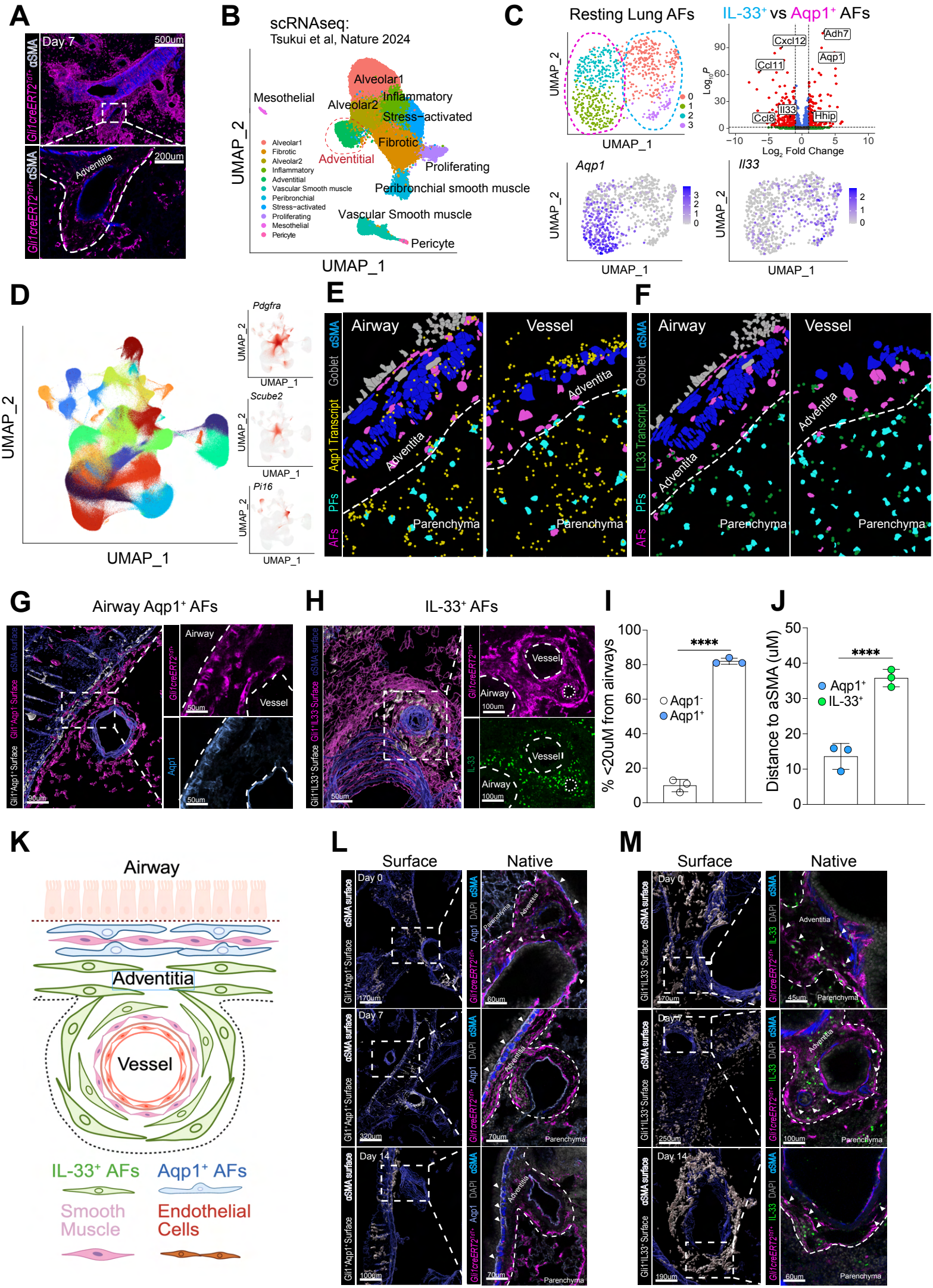
A
Day 7
500um
Gli1creERT2tdTr αSMA
200um
Adventitia
B
scRNAseq:
Tsukui et al, Nature 2024
Mesothelial
Alveolar1
Alveolar2
Inflammatory
Stress-activated
Fibrotic
Adventitial
Proliferating
Peribronchial smooth muscle
Vascular Smooth muscle
Pericyte
Alveolar1
Fibrotic
Alveolar2
Inflammatory
Adventitial
Vascular Smooth muscle
Peribronchial
Stress-activated
Proliferating
Mesothelial
Pericyte
UMAP_2
UMAP_1
C
Resting Lung AFs
IL-33+ vs Aqp1+ AFs
Cxcl12
Adh7
Aqp1
Ccl11
Il33
Ccl8
Hhip
Log10P
Log2 Fold Change
Aqp1
Il33
UMAP_2
UMAP_1
D
Pdgfra
Scube2
Pi16
UMAP_2
UMAP_1
E
Airway
Vessel
αSMA
Goblet
Aqp1 Transcript
PFs
AFs
Adventitia
Parenchyma
F
Airway
Vessel
αSMA
Goblet
IL33 Transcript
PFs
AFs
Adventitia
Parenchyma
G
Airway Aqp1+ AFs
Gli1+Aqp1+Surface
αSMA surface
Airway
Vessel
Aqp1
90um
50um
H
IL-33+ AFs
Gli1+IL33+Surface
αSMA surface
Vessel
Airway
IL-33
50um
100um
I
% <20uM from airways
****
Aqp1-
Aqp1+
J
Distance to aSMA (uM)
****
Aqp1+
IL-33+
K
Airway
Adventitia
Vessel
IL-33+ AFs
Aqp1+ AFs
Smooth Muscle
Endothelial Cells
L
Surface
Native
Day 0
Day 7
Day 14
αSMA surface
Gli1+Aqp1+Surface
αSMA
DAPI
Aqp1
Gli1creERT2tdTr
Adventitia
Parenchyma
170um
60um
320um
70um
1000um
M
Surface
Native
Day 0
Day 7
Day 14
αSMA surface
Gli1+IL33+Surface
αSMA
DAPI
IL-33
Gli1creERT2tdTr
Adventitia
Parenchyma
170um
45um
250um
100um
190um
60um

Figure 3

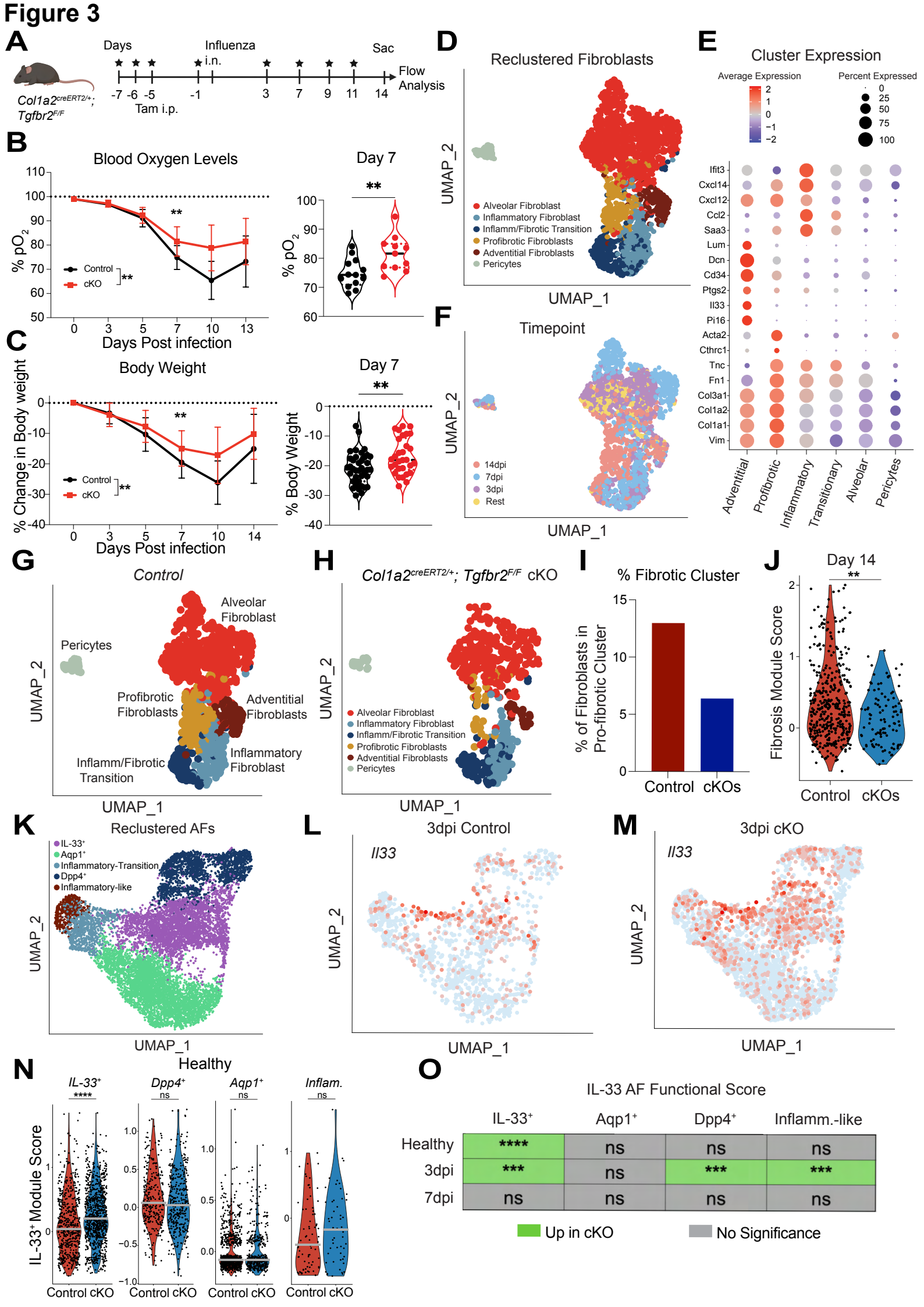
A
Days
Influenza i.n.
Sac
Flow Analysis
-7 -6 -5 -1 3 7 9 11 14
Tam i.p.
Col1a2creERT2/+; Tgfbr2F/F
B
Blood Oxygen Levels
% pO2
Control
cKO
Days Post infection
Day 7
C
Body Weight
% Change in Body weight
% Body Weight
D
Reclustered Fibroblasts
UMAP_2
UMAP_1
Alveolar Fibroblast
Inflammatory Fibroblast
Inflamm/Fibrotic Transition
Profibrotic Fibroblasts
Adventitial Fibroblasts
Pericytes
E
Cluster Expression
Average Expression
Percent Expressed
Ifit3
Cxcl14
Cxcl12
Ccl2
Saa3
Lum
Dcn
Cd34
Ptgs2
Il33
Pi16
Acta2
Cthrc1
Tnc
Fn1
Col3a1
Col1a2
Col1a1
Vim
Adventitial
Profibrotic
Inflammatory
Transitionary
Alveolar
Pericytes
F
Timepoint
14dpi
7dpi
3dpi
Rest
G
Control
Alveolar Fibroblast
Pericytes
Profibrotic Fibroblasts
Adventitial Fibroblasts
Inflammatory Fibroblast
Inflamm/Fibrotic Transition
H
Col1a2creERT2/+; Tgfbr2F/F cKO
I
% Fibrotic Cluster
% of Fibroblasts in Pro-fibrotic Cluster
Control
cKOs
J
Day 14
Fibrosis Module Score
K
Reclustered AFs
IL-33+
Aqp1+
Inflammatory-Transition
Dpp4+
Inflammatory-like
L
3dpi Control
Il33
M
3dpi cKO
N
Healthy
IL-33+
Dpp4+
Aqp1+
Inflam.
IL-33+ Module Score
Control cKO
O
IL-33 AF Functional Score
IL-33+
Aqp1+
Dpp4+
Inflamm.-like
Healthy
3dpi
7dpi
Up in cKO
No Significance

Figure S3

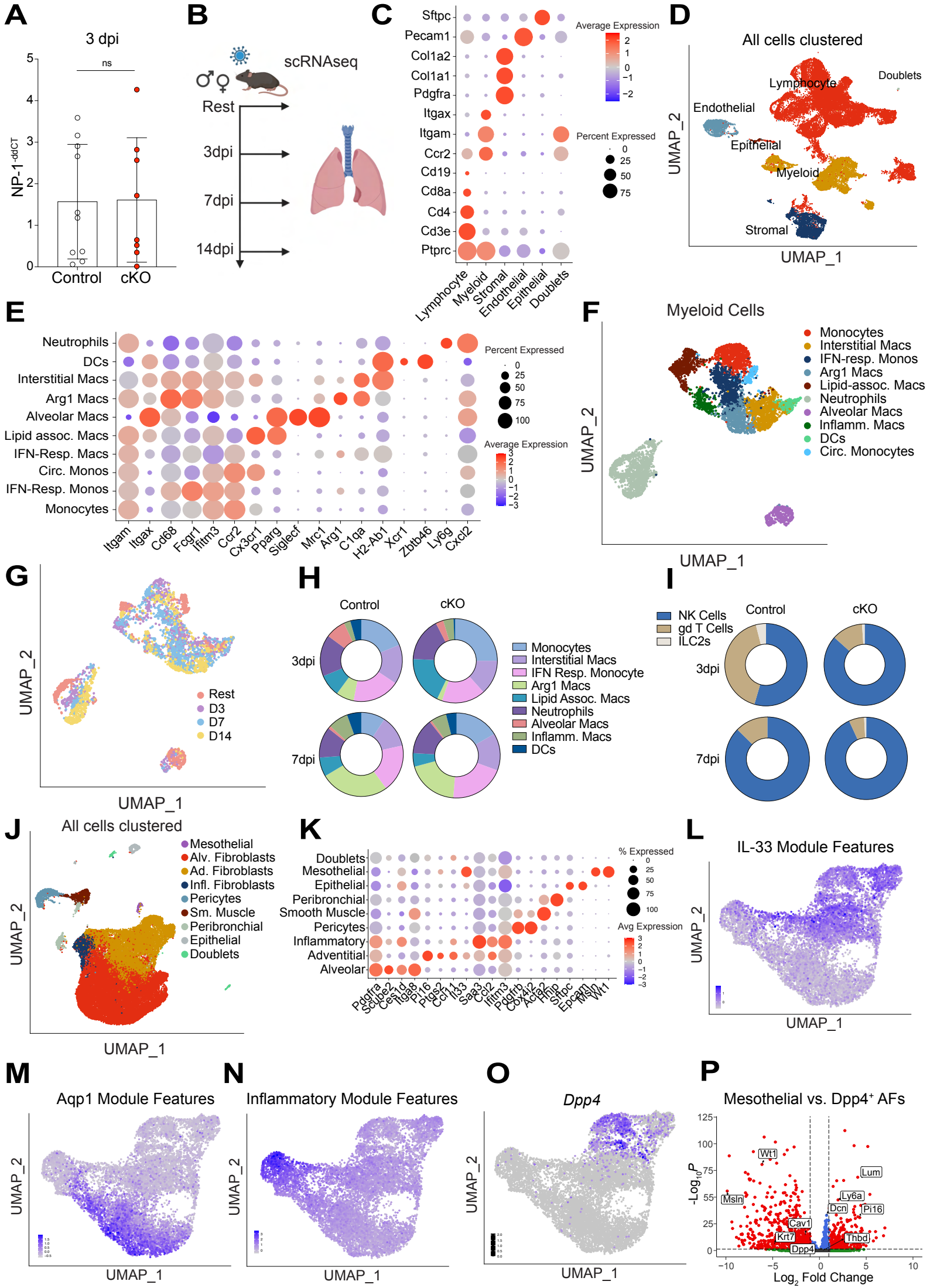
A
3 dpi
ns
NP-1-ddCT
Control
cKO
B
scRNAseq
Rest
3dpi
7dpi
14dpi
C
Sftpc
Pecam1
Col1a2
Col1a1
Pdgfra
Itgax
Itgam
Ccr2
Cd19
Cd8a
Cd4
Cd3e
Ptprc
Lymphocyte
Myeloid
Stromal
Endothelial
Epithelial
Doublets
Average Expression
Percent Expressed
D
All cells clustered
Lymphocyte
Doublets
Endothelial
Epithelial
Myeloid
Stromal
UMAP_2
UMAP_1
E
Neutrophils
DCs
Interstitial Macs
Arg1 Macs
Alveolar Macs
Lipid assoc. Macs
IFN-Resp. Macs
Circ. Monos
IFN-Resp. Monos
Monocytes
Itgam
Itgax
Cd68
Fcgr1
Ifitm3
Ccr2
Cx3cr1
Pparg
Siglecf
Mrc1
Arg1
C1qa
H2-Ab1
Xcr1
Zbtb46
Ly6g
Cxcl2
Percent Expressed
Average Expression
F
Myeloid Cells
Monocytes
Interstitial Macs
IFN-resp. Monos
Arg1 Macs
Lipid-assoc. Macs
Neutrophils
Alveolar Macs
Inflamm. Macs
DCs
Circ. Monocytes
UMAP_2
UMAP_1
G
Rest
D3
D7
D14
UMAP_2
UMAP_1
H
Control
cKO
3dpi
7dpi
Monocytes
Interstitial Macs
IFN Resp. Monocyte
Arg1 Macs
Lipid Assoc. Macs
Neutrophils
Alveolar Macs
Inflamm. Macs
DCs
I
NK Cells
gd T Cells
ILC2s
Control
cKO
3dpi
7dpi
J
All cells clustered
Mesothelial
Alv. Fibroblasts
Ad. Fibroblasts
Infl. Fibroblasts
Pericytes
Sm. Muscle
Peribronchial
Epithelial
Doublets
UMAP_2
UMAP_1
K
Doublets
Mesothelial
Epithelial
Peribronchial
Smooth Muscle
Pericytes
Inflammatory
Adventitial
Alveolar
Pdgfra
Scube2
Cec1d
Itga8
Pi16
Ptgs2
Ccl11
Il33
Saa3
Ccl2
Ifitm3
Pdgfrb
Cbx4l2
Acta2
Hhip
Sftpc
Epcam
Msln
Wt1
% Expressed
Avg Expression
L
IL-33 Module Features
UMAP_2
UMAP_1
M
Aqp1 Module Features
UMAP_2
UMAP_1
N
Inflammatory Module Features
UMAP_2
UMAP_1
O
Dpp4
UMAP_2
UMAP_1
P
Mesothelial vs. Dpp4+ AFs
Wt1
Lum
Msln
Ly6a
Dcn
Pi16
Cav1
Krt7
Thbd
Dpp4
-Log10 P
Log2 Fold Change

Figure 4

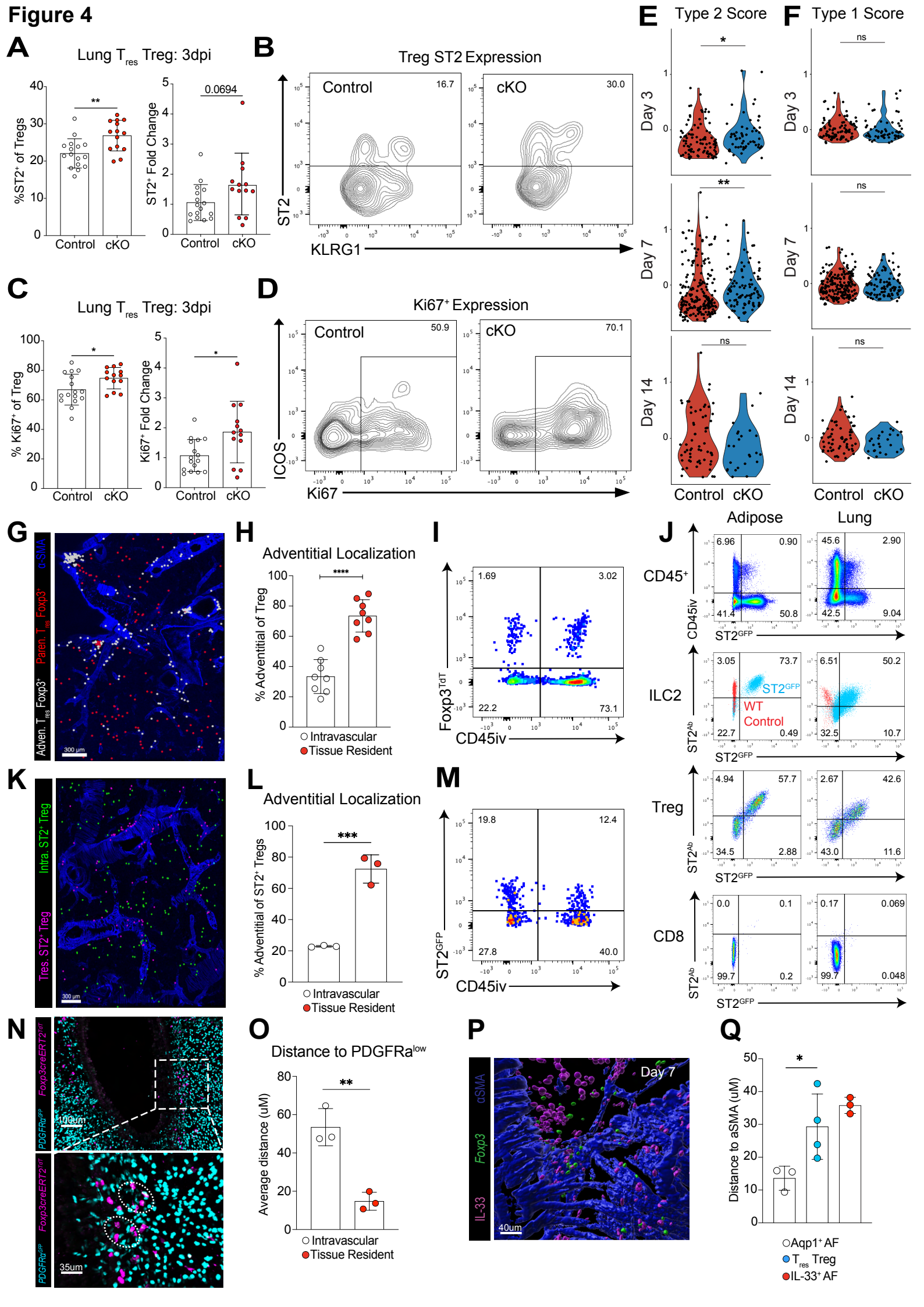
A
Lung T res Treg: 3dpi
%ST2+ of Tregs
ST2+ Fold Change
0.0694
Control
cKO
B
Treg ST2 Expression
Control
16.7
cKO
30.0
ST2
KLRG1
C
Lung T res Treg: 3dpi
% Ki67+ of Treg
Ki67+ Fold Change
D
Ki67+ Expression
Control
50.9
cKO
70.1
ICOS
Ki67
E
Type 2 Score
F
Type 1 Score
Day 3
Day 7
Day 14
ns
Control
cKO
G
α-SMA
Paren. T res Foxp3+
Adven. T res Foxp3+
300 µm
H
Adventitial Localization
% Adventitial of Treg
Intravascular
Tissue Resident
I
1.69
3.02
22.2
73.1
Foxp3TdT
CD45iv
J
Adipose
Lung
CD45+
CD45iv
ST2GFP
6.96
0.90
41.4
50.8
45.6
2.90
42.5
9.04
ILC2
ST2Ab
3.05
73.7
22.7
0.49
6.51
50.2
32.5
10.7
WT
Control
Treg
4.94
57.7
34.5
2.88
2.67
42.6
43.0
11.6
CD8
0.0
0.1
99.7
0.2
0.17
0.069
99.7
0.048
K
Intra. ST2+ Treg
Tres. ST2+ Treg
300 µm
L
Adventitial Localization
% Adventitial of ST2+ Tregs
Intravascular
Tissue Resident
M
19.8
12.4
27.8
40.0
ST2GFP
CD45iv
N
Foxp3creERT2TdT
PDGFRαGFP
100um
35um
O
Distance to PDGFRalow
Average distance (uM)
Intravascular
Tissue Resident
P
αSMA
Foxp3
IL-33
Day 7
40um
Q
Distance to aSMA (uM)
Aqp1+ AF
T res Treg
IL-33+ AF

Figure S4

No Significance | Up in cKO | Down in cKO

A

	Rest		Day 3		Day 7		Day 14	
	Ctrl	cKO	Ctrl	cKO	Ctrl	cKO	Ctrl	cKO
Neutrophil	16.05	19.58	11.61	12.23	14.44	17.99	11.95	13.05
NK Cells	12.27	11.53	10.13	11.48	6.77	5.98	5.25	5.21
Eosinophil	0.35	0.31	0.14	0.05	0.02	0.02	0.95	0.47
Alv. Macs	4.79	3.42	2.59	1.98	0.05	0.04	0.76	2.11
cDC1	0.17	0.18	0.29	0.31	0.18	0.12	0.29	0.31
cDC2	0.19	0.17	0.16	0.17	0.05	0.03	0.16	0.17
Macs	7.16	8.29	7.31	6.76	1.75	1.29	2.81	2.83
Monocyte	1.58	1.35	12	10.56	21.24	18.48	3.74	2.14
ILC2s	0.84	0.77	0.49	0.46	0.19	0.19	0.41	0.44
gd T cells	1.67	1.31	0.91	0.88	0.76	0.63	0.59	0.48
CD8	9.74	9.46	9.94	9.16	13.9	12.09	31.86	26.4
CD4	11.3	8.99	8.84	10.91	6.71	7.04	17.82	18.45
B Cells	6.4	4	10.23	10.24	6.42	7.87	11.73	14.24

B

	Ctrl	cKO	
Type 1 Tregs	14.78	15.33	Day 3
Type 1 CD4	37.48	36.83	
Type 2 CD4	5.58	5.42	
Type 1 Tregs	25.35	24.69	Day 7
Type 1 CD4	46.4	47.1	
Type 2 CD4	3.91	3.84	
Type 1 Tregs	43.95	44.44	Day 14
Type 1 CD4	50.87	59.71	
Type 2 CD4	0.97	1.08	

C

	Rest		Day 3		Day 7		Day 14	
	Ctrl	cKO	Ctrl	cKO	Ctrl	cKO	Ctrl	cKO
Neutrophil	1.92E+05	2.14E+05	1.50E+05	2.05E+05	1.89E+05	2.55E+05	1.34E+05	2.39E+05
NK Cells	1.36E+05	1.17E+05	1.70E+05	1.81E+05	2.32E+05	2.43E+05	1.08E+05	9.13E+04
Eosinophil	4.35E+03	3.51E+03	1.91E+03	2.15E+03	1.74E+02	3.10E+02	2.32E+04	6.34E+04
Alv. Macs	5.72E+04	3.79E+04	6.77E+03	6.15E+03	5.93E+02	5.34E+02	3.30E+03	4.57E+03
cDC1	2.07E+03	2.03E+03	1.75E+03	1.69E+03	1.77E+03	1.47E+03	3.89E+02	4.51E+02
cDC2	2.89E+03	1.88E+03	4.28E+02	3.19E+02	5.39E+02	4.24E+02	3.16E+03	3.34E+03
Macs	8.49E+04	8.37E+04	4.74E+04	3.95E+04	2.04E+04	1.73E+04	1.45E+04	1.57E+04
Monocyte	2.00E+04	1.44E+04	1.13E+05	1.01E+05	2.53E+05	2.45E+05	2.73E+04	3.48E+04
ILC2s	1.58E+04	1.55E+04	1.42E+04	1.45E+04	6.96E+03	7.58E+03	8.48E+03	6.48E+03
gd T cells	3.08E+04	2.44E+04	2.39E+04	2.20E+04	2.86E+04	2.36E+04	1.25E+04	1.08E+04
CD8	1.83E+05	1.93E+05	3.09E+05	2.78E+05	5.76E+05	4.61E+05	9.96E+05	7.17E+05
CD4	2.07E+05	1.76E+05	2.72E+05	3.15E+05	2.48E+05	2.60E+05	5.00E+05	3.58E+05
B Cells	1.21E+05	7.20E+04	3.05E+05	3.01E+05	2.32E+05	3.12E+05	3.32E+05	4.55E+05

D

	Ctrl	cKO	
Type 1 Tregs	1.79E+03	2.00E+03	Day 3
Type 1 CD4	2.34E+04	2.86E+04	
Type 2 CD4	2.89E+03	4.47E+03	
Type 1 Tregs	8.53E+03	7.71E+03	Day 7
Type 1 CD4	6.48E+04	6.85E+04	
Type 2 CD4	6.27E+03	6.66E+03	
Type 1 Tregs	2.08E+04	1.67E+04	Day 14
Type 1 CD4	2.86E+05	2.94E+05	
Type 2 CD4	5.53E+03	5.10E+03	

E

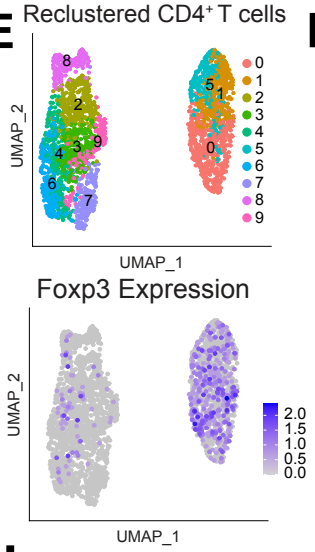

F

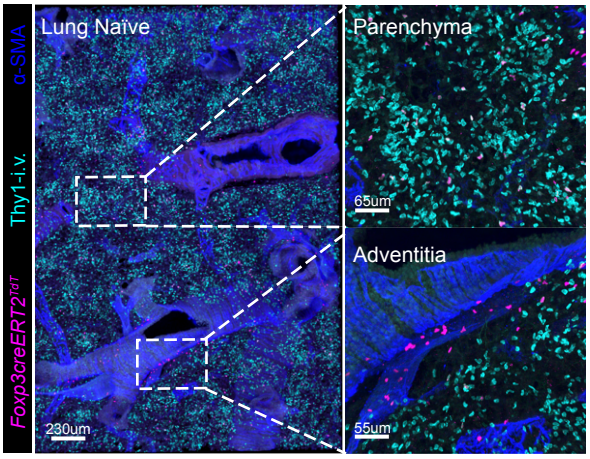

G

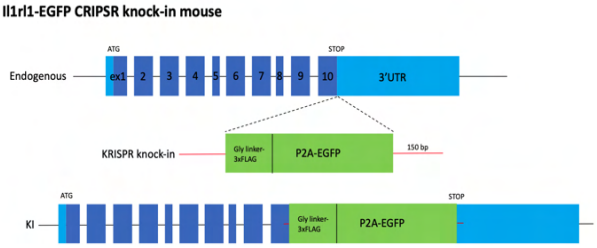

H

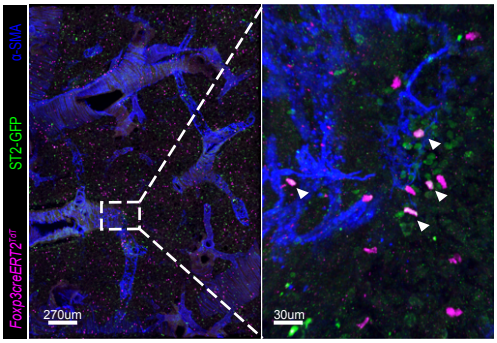

I

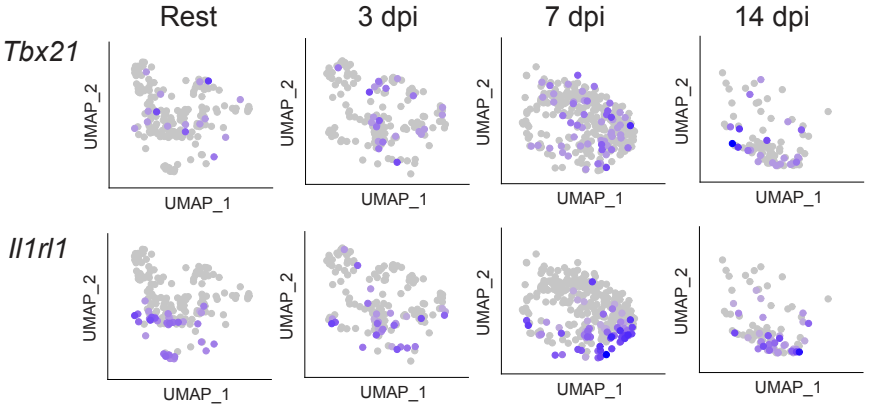

J

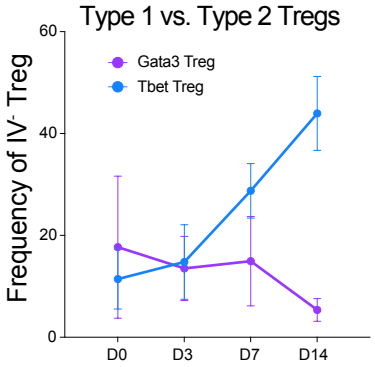

K

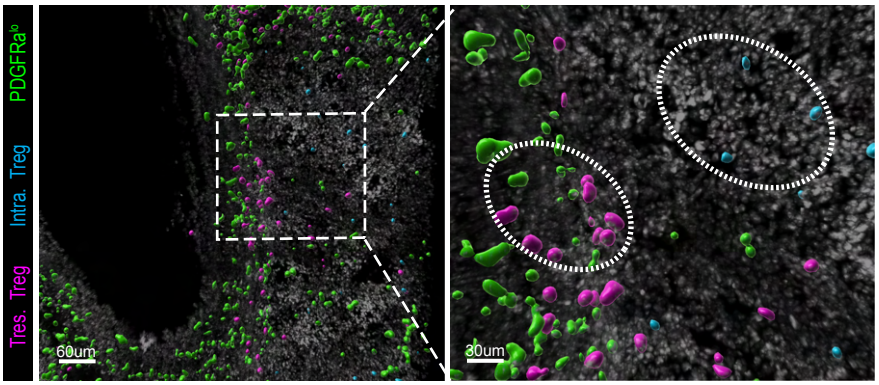

Figure 5

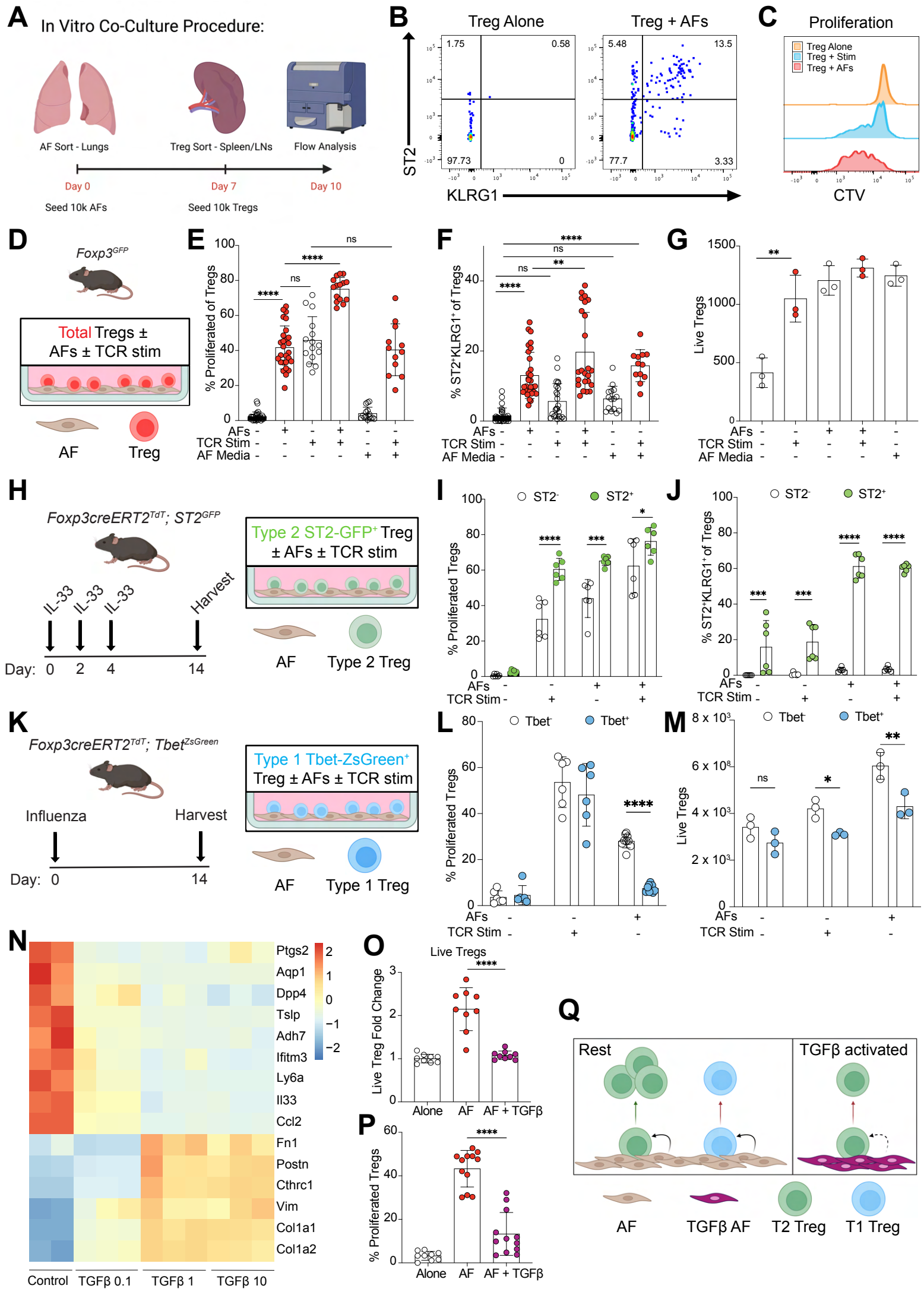
A
In Vitro Co-Culture Procedure:
AF Sort - Lungs
Treg Sort - Spleen/LNs
Flow Analysis
Day 0
Day 7
Day 10
Seed 10k AFs
Seed 10k Tregs
B
Treg Alone
Treg + AFs
ST2
KLRG1
1.75
0.58
97.73
0
5.48
13.5
77.7
3.33
C
Proliferation
Treg Alone
Treg + Stim
Treg + AFs
CTV
D
Foxp3GFP
Total Tregs ± AFs ± TCR stim
AF
Treg
E
% Proliferated of Tregs
AFs
TCR Stim
AF Media
F
% ST2+KLRG1+ of Tregs
G
Live Tregs
H
Foxp3creERT2TdT; ST2GFP
IL-33
IL-33
IL-33
Harvest
Day: 0 2 4 14
Type 2 ST2-GFP+ Treg ± AFs ± TCR stim
AF
Type 2 Treg
I
ST2-
ST2+
% Proliferated Tregs
J
% ST2+KLRG1+ of Tregs
K
Foxp3creERT2TdT; TbetZsGreen
Influenza
Harvest
Day: 0 14
Type 1 Tbet-ZsGreen+ Treg ± AFs ± TCR stim
AF
Type 1 Treg
L
Tbet-
Tbet+
% Proliferated Tregs
M
Live Tregs
N
Ptgs2
Aqp1
Dpp4
Tslp
Adh7
Ifitm3
Ly6a
Il33
Ccl2
Fn1
Postn
Cthrc1
Vim
Col1a1
Col1a2
Control
TGFβ 0.1
TGFβ 1
TGFβ 10
O
Live Tregs
Live Treg Fold Change
Alone
AF
AF + TGFβ
P
% Proliferated Tregs
Q
Rest
TGFβ activated
AF
TGFβ AF
T2 Treg
T1 Treg

Figure S5

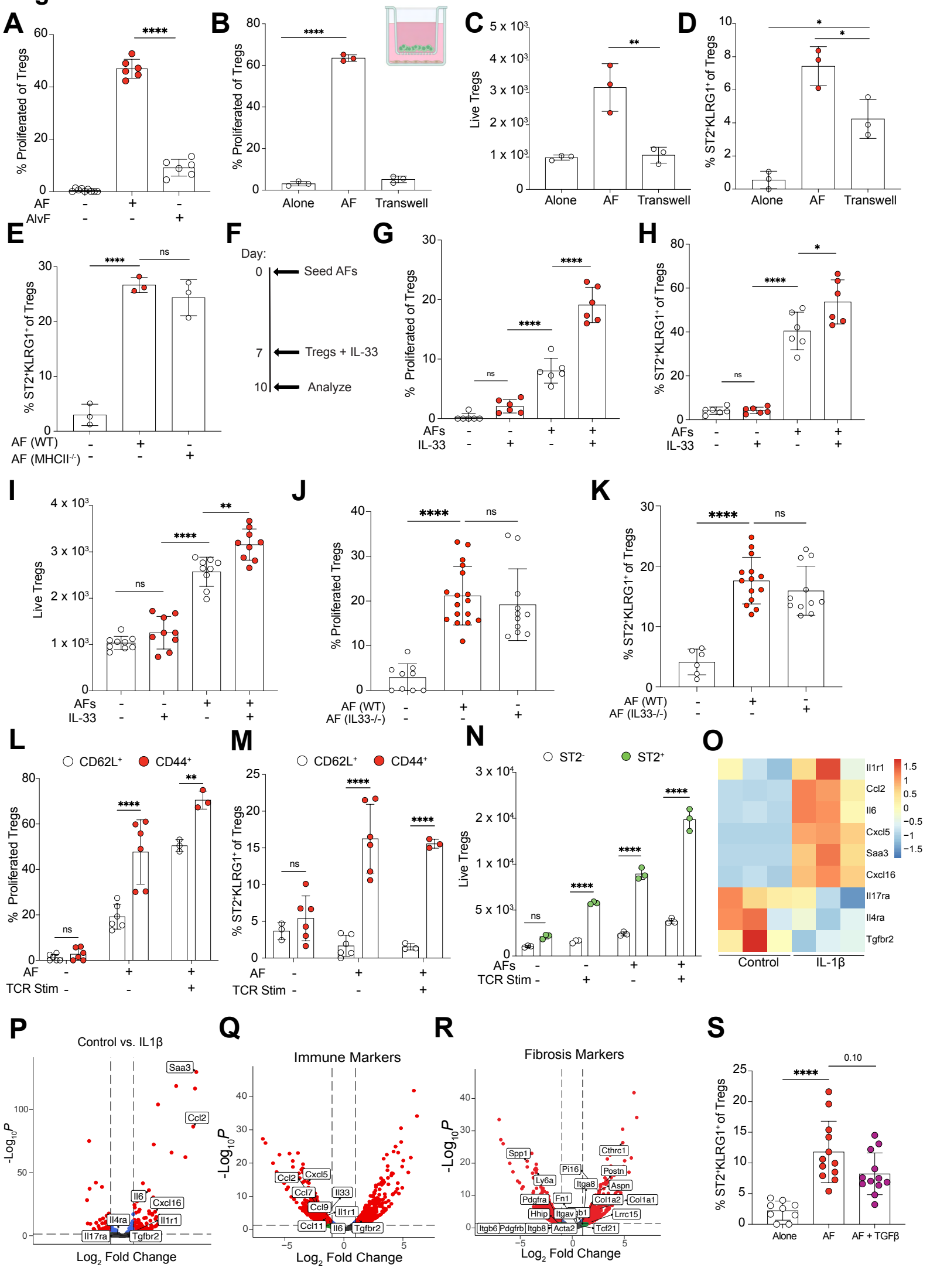
A
% Proliferated of Tregs
AF
AlvF
B
% Proliferated of Tregs
Alone
AF
Transwell
C
Live Tregs
Alone
AF
Transwell
D
% ST2+KLRG1+ of Tregs
Alone
AF
Transwell
E
% ST2+KLRG1+ of Tregs
AF (WT)
AF (MHCII-/-)
F
Day:
Seed AFs
Tregs + IL-33
Analyze
G
% Proliferated of Tregs
AFs
IL-33
H
% ST2+KLRG1+ of Tregs
AFs
IL-33
I
Live Tregs
AFs
IL-33
J
% Proliferated Tregs
AF (WT)
AF (IL33-/-)
K
% ST2+KLRG1+ of Tregs
AF (WT)
AF (IL33-/-)
L
CD62L+
CD44+
% Proliferated Tregs
AF
TCR Stim
M
CD62L+
CD44+
% ST2+KLRG1+ of Tregs
AF
TCR Stim
N
ST2-
ST2+
Live Tregs
AFs
TCR Stim
O
Il1r1
Ccl2
Il6
Cxcl5
Saa3
Cxcl16
Il17ra
Il4ra
Tgfbr2
Control
IL-1β
P
Control vs. IL1β
-Log10P
Log2 Fold Change
Saa3
Ccl2
Il6
Cxcl16
Il4ra
Il1r1
Il17ra
Tgfbr2
Q
Immune Markers
-Log10P
Log2 Fold Change
Ccl2
Cxcl5
Ccl7
Il33
Ccl9
Il1r1
Ccl11
Il6
Tgfbr2
R
Fibrosis Markers
-Log10P
Log2 Fold Change
Spp1
Cthrc1
Pi16
Postn
Ly6a
Itga8
Aspn
Pdgfra
Fn1
Col1a2
Col1a1
Hhip
Itgav
Lrrc15
Itgb6
Pdgfrb
Itgb8
Acta2
Tcf21
S
% ST2+KLRG1+ of Tregs
0.10
Alone
AF
AF + TGFβ

Figure 6

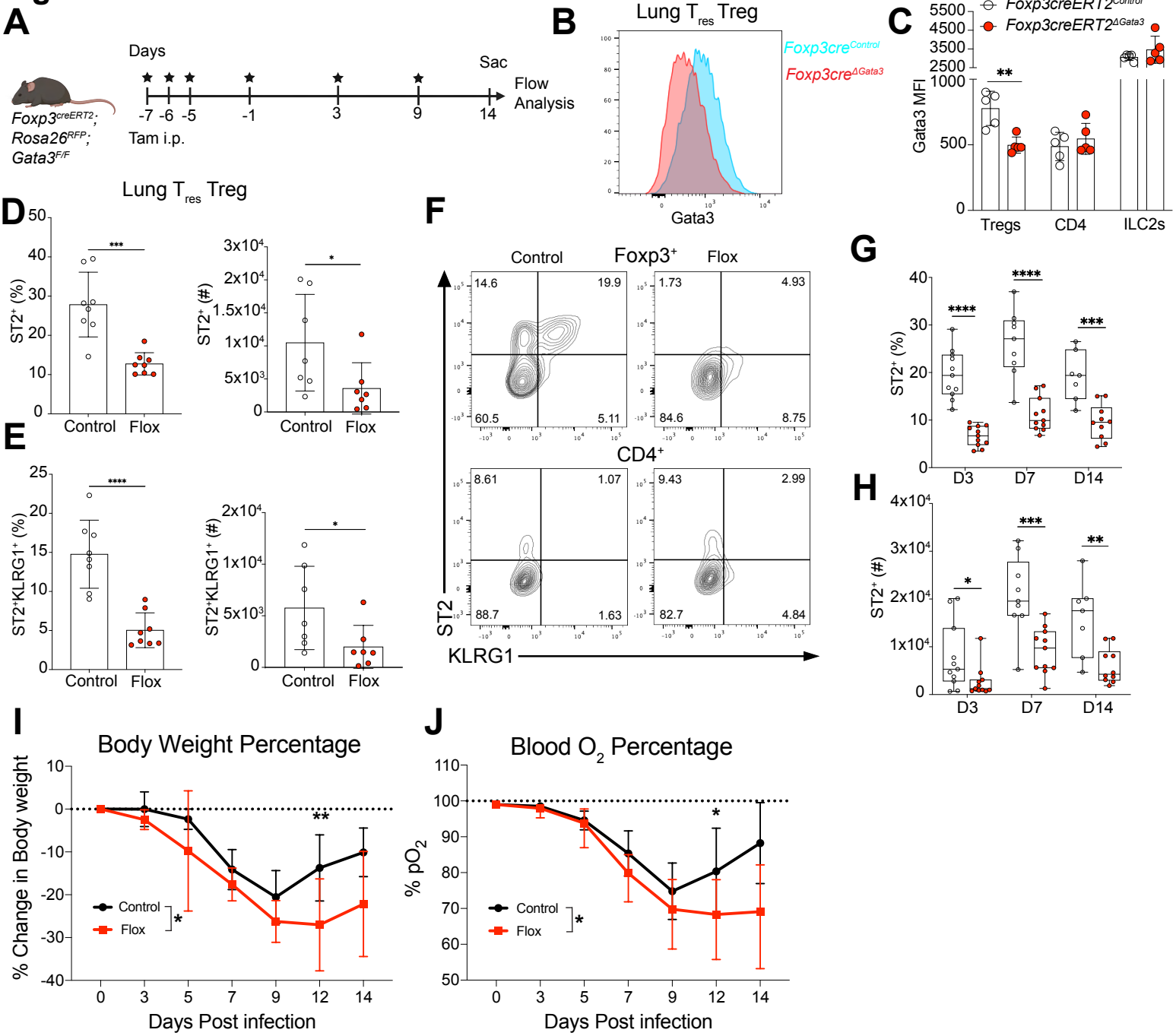
A
Days
Sac
Flow Analysis
-7 -6 -5 -1 3 9 14
Tam i.p.
Foxp3creERT2; Rosa26RFP; Gata3F/F
B
Lung Tres Treg
Foxp3creControl
Foxp3creΔGata3
Gata3
C
Foxp3creERT2Control
Foxp3creERT2ΔGata3
Gata3 MFI
Tregs
CD4
ILC2s
D
Lung Tres Treg
ST2+ (%)
ST2+ (#)
Control
Flox
E
ST2+KLRG1+ (%)
ST2+KLRG1+ (#)
F
Control
Foxp3+
Flox
CD4+
ST2
KLRG1
G
ST2+ (%)
D3
D7
D14
H
ST2+ (#)
I
Body Weight Percentage
% Change in Body weight
Control
Flox
Days Post infection
J
Blood O2 Percentage
% pO2
Days Post infection

Figure S6

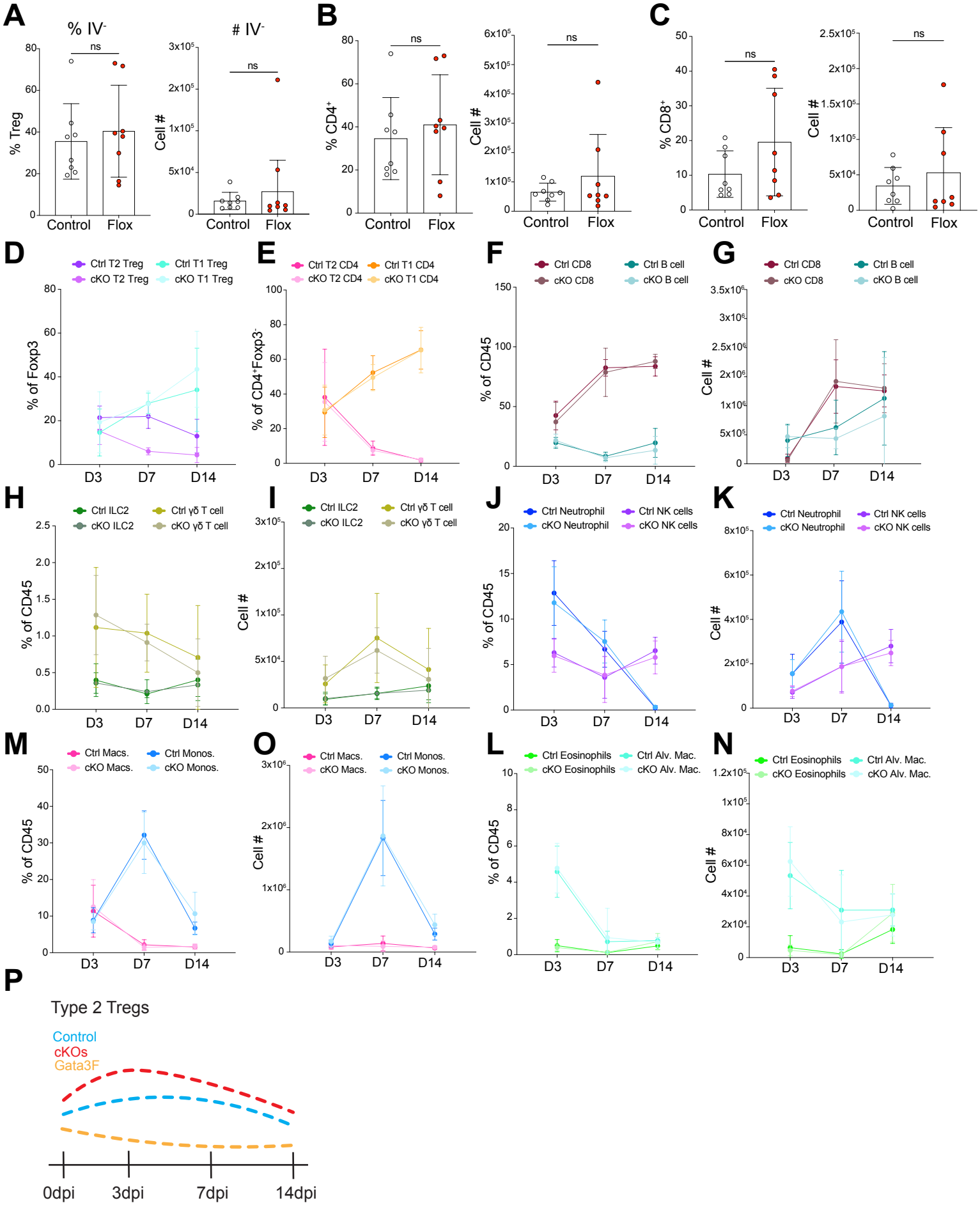
A
% IV-
# IV-
% Treg
Cell #
ns
Control
Flox
B
% CD4+
Cell #
C
% CD8+
D
Ctrl T2 Treg
Ctrl T1 Treg
cKO T2 Treg
cKO T1 Treg
% of Foxp3
E
Ctrl T2 CD4
Ctrl T1 CD4
cKO T2 CD4
cKO T1 CD4
% of CD4+Foxp3-
F
Ctrl CD8
Ctrl B cell
cKO CD8
cKO B cell
% of CD45
G
H
Ctrl ILC2
Ctrl γδ T cell
cKO ILC2
cKO γδ T cell
I
J
Ctrl Neutrophil
Ctrl NK cells
cKO Neutrophil
cKO NK cells
K
M
Ctrl Macs.
Ctrl Monos.
cKO Macs.
cKO Monos.
O
L
Ctrl Eosinophils
Ctrl Alv. Mac.
cKO Eosinophils
cKO Alv. Mac.
N
D3
D7
D14
P
Type 2 Tregs
Control
cKOs
Gata3F
0dpi
3dpi
7dpi
14dpi